Research Square

Preprints are preliminary reports that have not undergone peer review.
They should not be considered conclusive, used to inform clinical practice,
or referenced by the media as validated information.

Bacterial metalloproteinase-gated titanium implants enable on-demand infection control and osseointegration

Lin Wang

wanglin3@scut.edu.cn

South China University of Technology https://orcid.org/0000-0002-1880-1143

Wentao Zhang

https://orcid.org/0000-0003-4087-7280

Zhongyuan He

The Second Affiliated Hospital of Chongqing Medical University

Xinliang Peng

The Second Affiliated Hospital of Chongqing Medical University

Hang Zhou

The Second Affiliated Hospital of Chongqing Medical University

Zhaoyang Guo

The Second Affiliated Hospital of Chongqing Medical University

Ru Zhong

South China University of Technology

Meng Zhang

South China University of Technology

Zhongliang Deng

The Second Affiliated Hospital of Chongqing Medical University

Youliang Ren

University of Rochester Medical Center

Lei Chu

The Second Affiliated Hospital of Chongqing Medical University

Article

Keywords:

Posted Date: November 24th, 2026

DOI: https://doi.org/10.21203/rs.3.rs-11744314/v1

License: This work is licensed under a Creative Commons Attribution 4.0 International License.
Read Full License

Additional Declarations: There is **NO** Competing Interest.

Abstract

Implant-associated osteomyelitis frequently culminates in implant loosening and failure, yet current antibacterial implants either exhaust their antibiotic payload within days or impair bone integration through uncontrolled release. Here we report a titanium implant surface in which a bilayer titanium dioxide nanotube reservoir loaded with gentamicin sulfate is sealed by a bacterial metalloproteinase-responsive gatekeeper. After an initial prophylactic burst, the remaining antibiotic is retained for over 90 days and released on demand only upon enzymatic cleavage at infection-relevant protease concentrations, thereby spanning the entire subacute risk window, while gate-tethered sodium butyrate reprograms macrophages towards a pro-regenerative phenotype. In an in vivo delayed secondary infection model, the implant eradicated Staphylococcus aureus foci established 2 mm away even 30 days after implantation, attenuated inflammation and osteoclast activity, and achieved robust osseointegration, without compromising bone healing when infection never occurred. This infection-triggered, immunomodulatory platform offers protection across the full temporal spectrum of implant-associated infection.

1. Introduction

Titanium (Ti) implants are a cornerstone of modern orthopedic surgery, valued for their excellent biocompatibility and mechanical properties[1]. Despite these advantages, implant-associated osteomyelitis (IAO) remains a devastating complication that frequently culminates in implant loosening and failure, even with rigorous systemic and local antibiotic prophylaxis[2,3]. IAO complicates up to 2% of elective Ti-based joint replacements but afflicts an alarming 30% of internal fixations for open fractures[4], and its incidence continues to rise annually. The infection manifests predominantly within two distinct postoperative windows, namely an acute phase within 2 weeks that accounts for 60–70% of cases, and a subacute phase between 2 weeks and 3 months that accounts for 20–30% of cases[5,6]. Although both phases contribute to clinical failure, the subacute phase is particularly difficult to manage because it outlasts the protective window of most current antibacterial strategies. Once established, IAO is notoriously refractory to antibiotic therapy alone. Most patients inevitably require complex revision surgeries, often involving implant removal, at immense clinical and socioeconomic cost[7–9].

To pre-empt IAO, surface functionalization of titanium implants has emerged as a compelling strategy. Titanium dioxide nanotubes (TNT) produced by anodic oxidation represent a particularly attractive platform, as their high specific surface area permits efficient loading of diverse antimicrobial payloads and enables localized, precise drug release at the implantation site[10]. Despite these favorable properties, the translation of TNT-based antibacterial surfaces has been hindered by two interrelated limitations. Current TNT-based antibacterial surfaces typically rely on passive, sustained antibiotic release, which produces an initial burst followed by rapid depletion of the drug payload, leaving the entire subacute risk window inadequately protected[11,12]. This same unrestricted release profile also underlies the second limitation, namely intrinsic toxicity. Continuous, uncontrolled antibiotic exposure not only exhausts the

therapeutic reservoir prematurely but also induces local toxicity that severely impairs osseointegration[13]. Such toxicity is particularly detrimental during the subacute phase, when compromised bone healing can trigger a cascade of adverse outcomes, including heightened infection susceptibility, implant loosening, bone resorption, and loss of function. Therefore, a TNT implant surface capable of safeguarding the entire subacute period while simultaneously promoting robust bone integration remains an urgent and unmet clinical need.

Microenvironment-responsive gatekeepers offer a route to overcome these limitations by enabling infection-triggered, on-demand drug release with extended durations of action[14,15]. A key pathological feature of orthopaedic infections is the secretion of bacterial metalloproteinases (Bac-MPs) by predominant pathogens such as *Staphylococcus aureus* (*S. aureus*) and *Pseudomonas aeruginosa* (*P. aeruginosa*)[16 17]. Our epidemiological evidence from a 10-year multicentre cohort study confirmed that *S. aureus* (including *MSSA* and *MRSA*) and *P. aeruginosa* were among the most frequently isolated pathogens in post-traumatic limb osteomyelitis, with *P. aeruginosa* representing the most prevalent Gram-negative strain (10.92%)[18]. These findings underscore the clinical relevance of targeting Bac-MPs from these two pathogens in implant-associated infection scenarios. Bac-MPs actively dismantle tissue barriers by cleaving collagen, laminin, and fibronectin, thereby promoting bacterial invasion and dissemination[19], and they exacerbate local inflammation and tissue destruction by stimulating the release of pro-inflammatory mediators[20]. Given their pathogenic centrality and high local concentration during active infection, Bac-MPs represent a pathologically relevant trigger for responsive drug delivery[21]. Indeed, specific oligopeptide sequences, such as Gly-Pro-Leu-Gly-Met-Arg-Gly-Asp[22], undergo selective enzymatic cleavage upon Bac-MPs binding, and their hydrolysis efficiency correlates directly with Bac-MPs concentration[23,24].

To translate this enzymatic signal into a controllable release mechanism, a suitable gatekeeping molecule is required. Polyethylene glycol (PEG) stands out as an ideal candidate owing to its FDA-approved status, well-established clinical biosafety, and tunable physicochemical properties[25]. The *in vivo* residence time and barrier function of PEG can be precisely adjusted by modulating its degree of polymerization, enabling fine control over drug release kinetics[26,27]. When conjugated to the TNT surface through a Bac-MPs-cleavable peptide linker, PEG forms a protective corona that seals the antibiotic payload and prevents premature leakage. This design extends antibacterial protection into the subacute period while confining antibiotic release to episodes of active infection, thereby reducing the toxicity associated with constitutive exposure.

While infection-responsive release can mitigate antimicrobial toxicity, restoring and promoting osseointegration still requires an active biological component. Sodium butyrate (NaB) is an anti-inflammatory short-chain fatty acid that inhibits lipopolysaccharide-induced M1 macrophage polarization, dampens inflammation, and promotes a pro-regenerative M2 phenotype[28,29]. NaB also actively promotes osteoblast differentiation and bone formation by activating the Wnt/β-catenin signaling pathway and upregulating RUNX 2 expression, thereby directly enhancing interfacial

osseointegration[30,31]. When immobilized on the TNT surface, NaB can provide continuous anti-inflammatory and osteopromotive signals that complement the infection-responsive antibiotic release.

Building on the established role of Bac-MPs in orthopaedic infections, we designed a multi-functional TNT-based controlled-release system on titanium implant surfaces. This system integrates an enzyme-responsive peptide linker, a PEG-based gatekeeping molecule, and the anti-inflammatory osteopromotive agent NaB (Pep-PEG_{4000}-NaB, PPN). The design orchestrates a Bac-MPs-dependent enzyme-triggered unsealing cascade for precise spatiotemporal control over drug delivery. Specifically, the system releases an initial, sufficient burst of antibiotic to prevent acute postoperative infection, while the remaining antibiotic payload is sequestered within the nanotubes behind a protective PEG corona conjugated via the enzyme-responsive peptide. Only upon encountering the elevated Bac-MPs concentrations characteristic of an incipient infection does the peptide gatekeeper undergo cleavage, unsealing the TNT reservoir and triggering on-demand local antibiotic release precisely when and where it is needed. Concurrently, surface-immobilized NaB suppresses inflammation and actively promotes osseointegration, fostering a stable, long-term implant-bone interface. We systematically evaluated the *in vitro* responsive properties, antibacterial activity, and cytocompatibility of this implant, and further established a delayed infection animal model to assess its ability to prevent acute and subacute infections and promote osseointegration *in vivo*. This integrated strategy provides a platform to address the entire temporal spectrum of IAO risk while securing robust, durable implant integration.

2. Methods

2.1 Fabrication of single-layer and bi-layer titanium dioxide nanotubes

Pure Ti plates were cut into 10 x 5 cm^2 foils, and custom titanium screws were machined to the specified dimensions. All titanium substrates were ultrasonically cleaned twice in anhydrous ethanol for 5 min each, followed by ultrasonic cleaning in deionized water for 5 min, and then dried. The cleaned substrates were etched in 4% v/v hydrofluoric acid for 2 min to remove the native oxide layer, immediately rinsed with deionized water, ultrasonicated in anhydrous ethanol for 5 min, and dried.

The anodization electrolyte consisted of 0.3% w/v ammonium fluoride, 6% v/v deionized water, and 94% v/v ethylene glycol, and was thoroughly mixed before use. Anodization was performed in a two-electrode configuration with the treated titanium substrate as the anode and a cleaned graphite sheet as the cathode, using a DC power supply (Beijing Antaixin Technology Co., Ltd., China).

For single-layer titanium dioxide nanotubes, the voltage was held at 60 V for 24 min. For bilayer titanium dioxide nanotubes, the voltage was first held at 20 V for 6 min, then increased to 60 V at a constant rate of 15 V/min, and held at 60 V for an additional 18 min. After anodization, all substrates were repeatedly rinsed with deionized water to remove residual fluoride and then dried. The titanium foils were cut into 1 x 1 cm^2 pieces, ultrasonicated in anhydrous ethanol for 2 min, dried under nitrogen flow, and stored in a

desiccator. Samples with single-layer nanotubes were designated STNT, and those with bilayer nanotubes were designated TNT. Titanium screws subjected to the same bilayer anodization protocol were designated TNT-screws.

2.2 Drug loading

For Ti plate, gentamicin sulfate solutions at concentrations of 1, 2, 3, 4, 6, 8, and 12 mM were prepared in deionized water. A 35 μL aliquot of each solution was deposited onto the surface of prepared STNT or TNT samples. The samples were then placed in a vacuum drying oven for 90 min. This loading procedure was repeated for 24, 12, 8, 6, 4, 3, and 2 cycles corresponding to the respective gentamicin sulfate concentrations. After loading, the nanotube surfaces were rinsed with 1.5 mL of PBS to remove loosely adsorbed drug, and the rinse solutions were collected for quantification. The rinsed samples were dried and designated STNT@G for single-layer nanotubes and TNT@G for bilayer nanotubes. Gentamicin sulfate content in the rinse solutions was measured using a ninhydrin colorimetric assay, and the actual amount of drug loaded under each condition was calculated accordingly. The combination of 2 mM gentamicin sulfate and 12 loading cycles was selected as the optimal condition for subsequent experiments.

For TNT-screws, a 15 mM gentamicin sulfate solution was prepared in deionized water. Each screw was immersed in 150 μL of the solution and placed in a vacuum drying oven for 240 min. After loading, the screw surfaces were quickly rinsed with 1.5 mL of PBS to remove loosely adsorbed drug, and the rinse solutions were collected for quantification. The rinsed screws were dried and designated TNT@G-screws.

2.3 Immobilization of gating molecule

Pep-PEG_{4000}-NaB was dissolved in 95% ethanol at concentrations ranging from 20 to 70 μM. Drug-loaded samples (including both plates and screws) were immersed in 600 μL of the grafting solution and incubated for 1 to 6 h, respectively. Grafted surfaces were rinsed with PBS to remove physically adsorbed gating molecules. The wash solutions were collected, and the content of grafted gating molecules was quantified using a BCA assay to determine the grafting density at each time point. Based on these results, a combination of 50 μM Pep-PEG_{4000}-NaB and a 4 h incubation time was selected as the optimal condition for subsequent sample preparation. After grafting, the drug-loaded bilayer nanotube plates and screws were designated as TNT-PPN@G and TNT-PPN@G-screws, respectively. Unloaded bilayer nanotube plates and screws were also modified with Pep-PEG_{4000}-NaB under the same conditions and designated as TNT-PPN and TNT-PPN-screws, respectively. Drug-loaded single-layer nanotube samples were modified with Pep-PEG_{4000}-NaB under identical conditions and designated as STNT-PPN@G. Meanwhile, we employed gating molecule without NaB (Pep-PEG_{4000}, PP) as the control group, and the samples were designated as TNT-PP and TNT-PP@G.

2.4 *In vitro* drug release assay

Drug release was evaluated by placing samples in 24-well plates containing 500 μL of PBS per well and incubating them at 37°C. At predetermined time points, the release medium was collected and replaced with fresh PBS. For enzyme-responsive release studies, the PBS in selected wells was replaced with Bac-MPs solutions at concentrations of 2, 3, 4, 5, or 6 μg/mL to trigger drug release. Gentamicin sulfate concentrations in the collected solutions were quantified using a ninhydrin colorimetric assay, and cumulative release profiles were calculated over time. The same procedure was applied to compare single- and double-loaded samples, as well as for long-term release monitoring over 180 days.

2.5 *In vitro* antibacterial assay

2.5.1 Agar plate assay

Ti, TNT, TNT-PP, TNT-PPN, TNT@G, TNT-PP@G and TNT-PPN@G samples were placed in 24-well plates and inoculated with 35 μL of *S. aureus* (ATCC 6538p) or *P. aeruginosa* (ATCC 29213) suspension at 1 x 10^7 CFU/mL. After incubation at 37°C for 2 h, samples were transferred to centrifuge tubes containing 1 mL PBS and sonicated to detach adherent bacteria. A 10 μL aliquot of the resulting suspension was plated on agar, incubated at 37°C for 16 h, and colonies were counted to quantify antibacterial activity.

For cyclic antibacterial testing, Ti, TNT@G and TNT-PPN@G samples were inoculated with 40 μL of bacterial suspension at 1 x 10^4 CFU/mL and incubated in the dark at 37°C for 2 h. A 10 μL aliquot of the surface suspension was then plated for bacterial quantification. The sample surfaces were rinsed with PBS, dried, and the entire inoculation-incubation-counting procedure was repeated for six consecutive cycles to evaluate cyclic antibacterial performance.

2.5.2 SEM assay

For morphological observation of bacteria, Ti, TNT, TNT-PP, TNT-PPN, TNT@G, TNT-PP@G and TNT-PPN@G samples were inoculated as described above and incubated at 37°C for 2 h. Then, 600 μL of paraformaldehyde was slowly added along the well wall, and samples were fixed overnight at 4°C. After removing the fixative, samples were dehydrated through a graded ethanol series, followed by the addition of 600 μL tert-butanol and freeze-drying overnight. Dried samples were sputter-coated with gold for 60 s and imaged by SEM (SEM, JSM-6510LV, Japan) at an accelerating voltage of 5 kV under vacuum.

2.5.3 Live/dead assay

Ti, TNT, TNT-PP, TNT-PPN, TNT@G, TNT-PP@G and TNT-PPN@G samples were inoculated with 35 μL of *S. aureus* or *P. aeruginosa* suspension at 1 x 10^7 CFU/mL and incubated at 37°C for 2 h. After aspirating the bacterial suspension, 80 μL of propidium iodide and 160 μL of fluorescein diacetate were added and incubated for 5 min. Samples were then washed three times with deionized water, dried, and observed using an upright fluorescence microscope (DM6M, Leica, Germany) with FITC and TRITC channels to assess live/dead bacterial states.

2.5.4 Biofilm inhibition assay

Ti, TNT, TNT-PP, TNT-PPN, TNT@G, TNT-PP@G and TNT-PPN@G samples were inoculated with bacteria as described above and incubated at 37°C in the dark for 24 h. The culture medium was then replaced with 500 μL TSB medium, and incubation continued in the dark for an additional 48 h. After aspirating planktonic bacteria and residual medium, samples were rinsed twice with sterile PBS and stained with 0.1% crystal violet solution for 10 min. Following two PBS rinses, biofilm formation was qualitatively observed by bright-field microscopy. The crystal violet was then dissolved from the biofilms using anhydrous ethanol, and the absorbance of the resulting solution was measured at 590 nm with a microplate reader (FlexStation 3, Molecular Devices, USA) to quantify biofilm biomass.

2.5.5 Antibacterial activity of release solutions

Release solutions collected at days 1, 7, 30, 60, and 90 from the MMP-triggered release assay were tested for antibacterial activity. Bacterial suspensions of *S. aureus* and *P. aeruginosa* at 1 x 10^7 CFU/mL were prepared as described above. A 90 μL aliquot of each release solution was mixed with 10 μL of bacterial suspension to achieve a final concentration of 1 x 10^6 CFU/mL. After incubation at 37°C for 2 h, the suspensions were diluted with sterile PBS, and 10 μL of each dilution was spread on agar plates. Colonies were counted after incubation at 37°C for 16 h to determine the antibacterial activity of the release solutions at each time point.

2.5.6 Transcriptomic analysis of bacterial response

S. aureus suspensions at 1 x 10^7 CFU/mL were prepared as previously described. TNT and TNT-PPN@G samples were incubated in 500 μL of the bacterial suspension for 2 h, after which the samples were centrifuged at 1 x 10^4 rpm for 10 min to pellet the bacterial cells. Total bacterial RNA was then extracted using TRIzol reagent according to the manufacturer's instructions. RNA sequencing and differential gene expression analysis were performed.

2.6 *In vitro* cell assay

2.6.1 Cytocompatibility assay

For cell morphology assay, Ti, TNT, TNT-PP, TNT-PPN, TNT@G, TNT-PP@G and TNT-PPN@G samples were placed in 24-well plates. A 1 mL aliquot of human bone marrow mesenchymal stem cells (hBMSCs) suspension (2 x 10^4 cells/mL in α-MEM supplemented with 10% FBS) was added to each sample surface. Cells were cultured at 37°C in a CO_2 incubator with regular medium changes. At the indicated time points, samples were transferred to new 24-well plates and fixed with 600 μL of 4% paraformaldehyde overnight at 4°C. After two PBS rinses, cells were permeabilized with 300 μL of 0.1% Triton X-100 for 10 min, followed by two PBS rinses. Subsequently, 300 μL of F-actin staining solution was added, and samples were incubated in the dark at room temperature for 120 min. After two additional PBS rinses, 300 μL of DAPI staining solution was added, and samples were incubated in the dark at room temperature for 6.5 min. Cell morphology was observed using a fluorescence microscope (DM6M, Leica, Germany).

For the CCK-8 assay, cells were cultured on the Ti, TNT, TNT-PP, TNT-PPN, TNT@G, TNT-PP@G and TNT-PPN@G samples as described above. At the indicated time points, the samples were transferred to new 24-well plates. CCK-8 reagent was mixed with complete culture medium at a 1:10 ratio according to the manufacturer's instructions, and 380 μL of the working solution was added to each well. The plates were incubated in the dark at 37°C for 2 h. After incubation, 100 μL of the solution from each well was transferred to a 96-well plate, and the absorbance at 450 nm was measured with a microplate reader.

2.6.2 Osteogenic differentiation assay

For quantitative real-time reverse transcription polymerase chain reaction (qRT-PCR) assay, Ti, TNT, TNT-PP, TNT-PPN, TNT@G, TNT-PP@G and TNT-PPN@G samples were placed in 24-well plates. A 1 mL aliquot of hBMSCs suspension (2 x 10^4 cells/mL in normal medium) was added to each sample surface, and cells were cultured in a humidified incubator at 37°C with 5% CO_2. On day 3, the growth medium was replaced with osteogenic induction medium (α-MEM, 10% FBS, 50 μM ascorbic acid, 10 mM β-glycerophosphoric acid, and 1 x 10^{-5} mM dexamethasone). After 7 and 14 days of further culture, the samples were transferred to new 24-well plates. The expression of osteogenic marker genes was quantified by qRT-PCR to assess osteogenic differentiation (Table 1).

Table 1
Sequences of genes used in qRT-PCR.

Genes	**Sequences(5'-3')**
GAPDH-hF	TGGTGAAGCAGGCATCTGAG
GAPDH-hR	TGAAGTCGCAGGAGACAACC
ALP-hF	AGCACTCCCACTTCATCTGGAA
ALP-hR	GAGACCCAATAGGTAGTCCACATTG
COL I-hF	TTCGTGACCGTGACCTTGAG
COL I-hR	TCTCCGCTCTTCCAGTCAGA
OPN-hF	CTTTACAGCCTGCACCCAGA
OPN-hR	TTCTGTGGCGCAAGGAGATT
RUNX 2-hF	CCTCAGTGATTTAGGGCGCA
RUNX 2-hR	ACTTGGTGCAGAGTTCAGGG

For Alkaline phosphatase (ALP) staining assay, cells were cultured on the Ti, TNT, TNT-PP, TNT-PPN, TNT@G, TNT-PP@G and TNT-PPN@G samples as described above. At the indicated time points, the samples were transferred to new 24-well plates, and 300 μL of RIPA lysis buffer was added to each well. The plates were incubated at 4°C for 15 min. The lysates were then collected into centrifuge tubes and centrifuged at 1.2 x 10^4 rpm for 5 min at 4°C in a refrigerated centrifuge. The supernatants were

collected, and ALP activity was measured using an ALP activity assay kit according to the manufacturer's instructions. The absorbance was measured at 405 nm with a microplate reader, and the amount of p-nitrophenol produced was determined. Total protein concentration in the cell lysates was determined using a BCA protein assay kit. Relative ALP activity was calculated as the amount of p-nitrophenol normalized to total protein concentration.

For Alizarin red staining, the procedures for cell culture and fixation were consistent with those described for ALP staining. Fixed hBMSCs were stained with 1% Alizarin Red S (pH 4.2) for 5 min, followed by five washes with PBS. Stained samples were imaged using a stereo microscope (Stereo Discovery V20, ZEISS). For quantitative analysis, alizarin red was dissolved from the sample surfaces using chlordodecyl pyridine solution, and the absorbance was measured at 562 nm using a microplate reader.

2.6.3 Anti-inflammatory assay

For qRT-PCR, Ti, TNT, TNT-PP, TNT-PPN, TNT@G, TNT-PP@G and TNT-PPN@G samples were placed in 24-well plates, and 1 mL of RAW264.7 macrophage suspension (3 x 10^4 cells/mL in high-glucose medium) was added to each sample surface. Cells were cultured at 37°C in a humidified incubator with 5% CO_2. After 3 days, samples were transferred to fresh 24-well plates and rinsed twice with PBS. The expression of the inflammatory genes iNOS, TNF-α, IL-10, and IL-1β was quantified by qRT-PCR to assess inflammatory modulation by the materials (Table 2).

Table 2
Sequences of genes used in qRT-PCR.

Genes	Sequences(5'-3')
GAPDH-hF	AAATGGTGAAGGTCGGTGTGAAC
GAPDH-hR	CAACAATCTCCACTTTGCCACTG
iNOS-hF	CAAGCTGAACTTGAGCGAGGA
iNOS-hR	TTTACTCAGTGCCAGAAGCTGGA
TNF-α-hF	GGGATGAGAAGTTCCCAAAT
TNF-α-hR	AGGCTTGTCACTCGAATTTT
IL-10-hF	GCGCTGTCATCGATTTCTCC
IL-10-hR	AGGTCTTGTTACACTCGCCC
IL-1β-hF	GCTACCTGTGTCTTTCCCGT
IL-1β-hR	AATGGGAACGTCACACACCAG

For flow cytometry, Ti, TNT, TNT-PP, TNT-PPN, TNT@G, TNT-PP@G and TNT-PPN@G samples were placed in 24-well plates, and RAW264.7 macrophages were seeded onto each sample surface and cultured as

described above. After 3 days, samples were transferred to fresh 24-well plates, and adherent cells were harvested by trypsinization. Cells from each group were washed with PBS, collected by centrifugation, and resuspended in 100 μL of PBS. Fc receptor blocking reagent was added, and the cells were incubated at 4°C for 5 min. Subsequently, 1.2 μL of CD206 antibody was added, and the cells were incubated at 4°C for 30 min. Cells were washed three times with PBS by centrifugation and resuspension, and finally resuspended in 400 μL of PBS for flow cytometry analysis of M2 macrophage polarization.

2.7 *In vivo* assay

2.7.1 Model establishment

All animal procedures were approved by the Institutional Animal Care and Use Committee of Chongqing Medical University (protocol number IACUC-SAHCQMU-2025-0120). Male Sprague-Dawley rats (SD rats, n = 240, 250–300 g, 8–10 weeks) were used for *in vivo* experiments. Anesthesia was induced by intraperitoneal injection of pentobarbital sodium. The fur over the knee joint was shaved, and the skin was disinfected with iodophor. A skin incision was made over the lateral femoral condyle, and the fascia and underlying muscle were separated by blunt dissection to expose the condyle. A bicortical bone defect was then created in the lateral femoral condyle using a sterile 1.0-mm-diameter drill bit. Sterilized modified screws (referred to as Test Screws) were implanted into the defect and tightened, and the surgical site was irrigated with sterile saline. The muscle and skin were closed in layers to complete the initial implantation.

For the secondary infection model, a second bone defect was created 2.0 mm proximal to the implanted screw using a 1.0-mm-diameter drill at 7 (the early infection model) or 30 days (the late infection model) after the initial implantation. A sterile cotton swab saturated with *S. aureus* suspension (1 x 10^8 CFU/mL) was applied to the newly created defect three times, and the defect was then sealed with a sterile short screw (referred to as Infected Screws) to prevent bacterial leakage. Rats were euthanized 7 or 30 days after bacterial inoculation, and samples were collected.

For the non-infection model, screws were implanted without bacterial inoculation, and rats were euthanized 90 days after implantation for sample collection.

2.7.2 *In vivo* antibacterial assay

After euthanasia, femurs containing the implanted screws were harvested by carbon dioxide asphyxiation. The Test Screws with surrounding bone tissue and the adjacent Infected Screws with surrounding bone tissue were collected and placed in 1 mL of PBS. Samples were sonicated for 10 min and vortexed thoroughly. The resulting suspensions were diluted 10-fold in PBS, and 10 μL aliquots were spread onto agar plates. After incubation at 37°C for 16 h, colonies were counted to quantify the bacterial burden on and around the implant.

2.7.3 Histological assessment of inflammation

Femur samples were fixed in 4% paraformaldehyde, decalcified, dehydrated, and embedded in paraffin. Sections (5 μm thick) were prepared and stained with hematoxylin and eosin (H&E) for histological evaluation of inflammatory infiltration.

2.7.4 *In vivo* transcriptomic analysis

For the early infection model, femur samples were collected 7 days after bacterial inoculation. The implanted screws were removed, and bone segments adjacent to the implant were collected in 500 μL of PBS. Samples were sonicated for 3 min and centrifuged at 1 x 10^4 rpm for 10 min to pellet cells and bacteria. Total RNA was extracted using TRIzol reagent according to the manufacturer's instructions, and RNA sequencing and differential gene expression analysis were performed.

2.7.5 Osseointegration assay

Femur samples were fixed in 4% paraformaldehyde and scanned by micro-computed tomography (Micro-CT) to evaluate periprosthetic bone formation. Bone volume fraction (BV/TV) and bone mineral content (BMC) in the periprosthetic regions were quantified from the reconstructed images.

For undecalcified histology, femurs with implants were dehydrated through graded alcohols and xylene, embedded in methyl methacrylate, and ground and polished to produce hard tissue sections approximately 20 μm thick. Sections were stained with methylene blue and basic fuchsin to evaluate bone–implant contact (BIC).

For decalcified histology, samples were processed as described above, and sections were stained with H&E, Masson's trichrome, and tartrate-resistant acid phosphatase (Trap) to evaluate inflammation, collagen deposition, and osteoclast activity, respectively.

For systemic biocompatibility assessment, major organs (heart, liver, spleen, lung, and kidney) were collected from unchallenged animals 90 days after implantation, fixed in 4% paraformaldehyde, embedded in paraffin, sectioned, and stained with H&E to evaluate systemic toxicity.

2.8 Statistics analysis

All data were statistically analyzed using GraphPad Prism 8.0 Software. Values were presented as mean ± SD. An independent-sample t-test and one-way ANOVA were used for intergroup comparisons.

3. Results

3.1 Preparation and characterization of TNT-PPN@G

A bilayer titanium dioxide nanotube (TNT) array, comprising a narrow upper layer and a wider lower layer, was fabricated via a two-step anodization process (Fig. 1a). SEM revealed an ordered structure with an upper nanotube length of ~ 60 nm and pore diameters of 20 to 26 nm, situated above a ~ 1200 nm-thick lower layer with diameters of 50 to 70 nm (Fig. 1b, Fig. 1c and **Supplementary Figure S1**). This geometry

was maintained not only on planar titanium surfaces but also across the complex topography of orthopaedic screws, where the thread valleys and crests exhibited uniform TNT morphology (**Supplementary Figure S2**).

In the gentamicin sulfate loading experiments, the drug concentration and the number of loading cycles were varied while keeping their product constant, thereby ensuring that an equivalent total quantity of drug was introduced to each sample. Notably, the amount of drug loaded into the TNT was found to decrease with increasing drug solution concentration. The highest loading capacities were achieved under conditions of 1 mM with 24 cycles and 2 mM with 12 cycles (Fig. 1d). To optimize loading efficiency, we adopted the 2 mM, 12-cycle protocol for all subsequent gentamicin sulfate loading into TNT arrays (TNT@G).

Subsequent grafting of Pep-PEG_{4000} (PP) and Pep-PEG_{4000}-NaB (PPN) gating molecules followed saturation kinetics, with grafting density increasing as a function of both incubation time and solution concentration. The reaction plateaued after 4 h at a grafting solution concentration of 50 μM, yielding saturation densities of 0.68 molecules/nm^2 for PP and 0.67 molecules/nm^2 for PPN (Fig. 1e and **Supplementary Figure S3**). The resulting functionalized substrates are designated TNT-PP and TNT-PPN, respectively. Samples that were first loaded with gentamicin sulfate and subsequently immobilized with PP or PPN gating molecules are abbreviated as TNT-PP@G and TNT-PPN@G, respectively.

XPS analysis confirmed the successful immobilization of the PPN gate and the retention of gentamicin sulfate within the nanotubes. Relative to the pristine TNT surface, TNT-PPN spectrum exhibited an increased intensity of the C 1s signal, indicative of the grafted Pep-PEG_{4000} derivative (**Supplementary Figure S4**). Furthermore, the emergence of a distinct N 1s and Ti 2p signal on both TNT@G and TNT-PPN@G surfaces verified the presence of gentamicin sulfate within the nanotubular reservoirs, both prior to and following the immobilization of the PPN gating layer **(**Fig. 1f, Fig. 1g and **Supplementary Figure S4)**.

The surface wettability of the modified substrates was characterized by water contact angle measurements. Pristine Ti exhibited a contact angle of 53.0°, which decreased markedly to 26.5° for the anodized TNT surface, confirming that the nanotubular architecture substantially enhances hydrophilicity. Subsequent immobilization of PP or PPN gating molecules further reduced the contact angles to 22.3° and 21.7°, respectively. In contrast, drug-loaded variants, including TNT@G, TNT-PP@G, and TNT-PPN@G, displayed slightly higher contact angles of 38.0°, 31.4°, and 31.3°, respectively, although these values remained significantly lower than that of pristine Ti (Fig. 1h).

Mechanical integrity of the modified surfaces was assessed using a nano-ultrasonic mechanical tester. Exfoliation force measurements revealed values of 11.42 N for TNT, 11.93 N for TNT-PPN, and 12.13 N for TNT-PPN@G (**Supplementary Figure S5**), all of which exceed the clinically mandated threshold[32]. Furthermore, universal mechanical testing of pristine and TNT-modified titanium screws indicated that

the anodic oxidation process did not compromise the bulk mechanical properties of the implant (**Supplementary Figure S6**).

To characterize the enzyme-responsive release behavior of gentamicin sulfate from the gated TNT systems, the optimal concentration of Bac-MPs was first determined. Gradient concentration assays revealed that the total enzyme-triggered antibiotic release increased as the Bac-MPs concentration rose from 2 μg/mL to 5 μg/mL, plateauing thereafter between 5 μg/mL and 6 μg/mL (**Supplementary Figure S7**). Accordingly, a Bac-MPs concentration of 5 μg/mL was selected for all subsequent gating experiments. Then, we monitored the release profiles of gentamicin sulfate from the samples. For the ungated control of TNT@G, a burst release of 80.62 μg (approximately 100% of the loaded payload) occurred within the first 24 h, and subsequent addition of Bac-MPs elicited no further antibiotic liberation (Fig. 1i). In contrast, TNT-PP@G and TNT-PPN@G exhibited initial release of 34.68 μg and 36.65 μg, respectively, on day 1, with the remaining gentamicin sulfate sequestered within the nanotubes until enzymatic stimulation. Upon addition of Bac-MPs on day 7 (Fig. 1i), an additional 50.10 μg and 51.73 μg were released from TNT-PP@G and TNT-PPN@G, respectively. The cumulative released amounts indicated that the total drug loading in TNT-PP@G (≥ 87.12 μg) and TNT-PPN@G (≥ 90.89 μg) was comparable to that of TNT@G, confirming that the immobilization of the PP or PPN gating layers did not compromise the drug-loading capacity of the TNT arrays.

This enzyme-responsive gating behaviour persisted over extended periods. Delayed addition of Bac-MPs on days 15, 30, 45, 60, and 90 triggered additional gentamicin sulfate release of 45.24, 38.14, 34.98, 33.92, and 11.87 μg from TNT-PP@G, and 47.71, 41.14, 35.02, 33.51, and 10.10 μg from TNT-PPN@G, respectively (Fig. 1i and **Supplementary Figure S8**). Notably, by day 180, stimulation with 5 μg/mL Bac-MPs produced no detectable antibiotic release, indicating complete depletion of the stored payload. Collectively, these data demonstrated that the PP and PPN gated TNT systems could effectively retain gentamicin sulfate for a period exceeding 90 days, thereby spanning the entire subacute phase of potential implant-associated infection.

A comparative analysis of the bilayer TNT architecture employed herein with a conventional single-layer TNT (STNT) variant was also performed. Exfoliation force measurements revealed that STNT possessed a lower mechanical resilience (9.42 N) than the bilayer TNT (11.42 N) (**Supplementary Figure S5**). Although the PPN-gated STNT (STNT-PPN@G) also exhibited enzyme-responsive release, the total drug-loading capacities of both ungated and gated STNT systems were substantially inferior to their bilayer TNT counterparts (**Supplementary Figure S9**). These findings established that the bilayer TNT configuration offered superior mechanical robustness and a greater drug-loading reservoir compared with the single-layer analogue.

3.2 *In vitro* antibacterial assay

To evaluate the antibacterial activity of the gated TNT systems against clinically relevant orthopedic pathogens, *S. aureus* and *P. aeruginosa* were employed as model organisms (Fig. 2a). Preliminary

characterization confirmed that both bacterial strains constitutively secrete Bac-MPs, with secreted enzyme levels increasing as a function of bacterial density (**Supplementary Figure S10**), thereby establishing the biochemical prerequisite for enzymatic gate opening.

Surfaces lacking gentamicin sulfate, including pristine Ti, TNT, TNT-PP, and TNT-PPN, exhibited negligible antibacterial activity, whereas all gentamicin sulfate-loaded groups, specifically TNT@G, TNT-PP@G, and TNT-PPN@G, achieved near-complete bacterial eradication against both *S. aureus* and *P. aeruginosa* within a 2 h incubation period (Fig. 2b). This result demonstrated that the initial burst release of gentamicin sulfate from both ungated TNT@G and gated TNT-PP@G or TNT-PPN@G was sufficient to inhibit bacterial infection, even though less gentamicin sulfate was released from the gated groups, meeting the antibacterial demands of the early acute infection stage. Moreover, cyclic antibacterial challenge assays revealed that the gated systems maintained potent bactericidal activity over four consecutive exposure cycles, TNT-PPN@G retaining an antibacterial rate of up to 94.33% by the fourth cycle (Fig. 2c).

Morphological examination by SEM revealed marked structural deterioration on these antibacterial surfaces. *S. aureus*, normally spherical and turgid, appeared deflated with evidence of intracellular content leakage, whereas *P. aeruginosa* rods became shortened and exhibited pronounced surface wrinkling (Fig. 2d). Complementary live/dead fluorescence staining corroborated these findings. Bacteria adherent to non-loaded surfaces, namely Ti, TNT, TNT-PP, and TNT-PPN, displayed uniform green fluorescence indicative of intact membrane integrity, whereas those on gentamicin sulfate-loaded substrates, specifically TNT@G, TNT-PP@G, and TNT-PPN@G, exhibited extensive red fluorescence, confirming compromised viability (**Supplementary Figure S11**).

The capacity of the functionalized surfaces to suppress biofilm establishment was assessed using crystal violet staining following 72 h of culture. Robust biofilm biomass developed on all gentamicin sulfate-free control surfaces for both *S. aureus* and *P. aeruginosa*. Conversely, biofilm accumulation was drastically reduced on all gentamicin sulfate-loaded variants, including TNT@G, TNT-PP@G, and TNT-PPN@G (Fig. 2e). Quantitative analysis demonstrated that, relative to Ti control, *S. aureus* biofilm biomass was diminished by 53.15%, 51.93%, and 49.05% on TNT@G, TNT-PP@G, and TNT-PPN@G, respectively, while *P. aeruginosa* biofilm was reduced by 65.96%, 63.63%, and 60.34%, respectively (Fig. 2f).

Additionally, long-term release experiments were performed in parallel with antibacterial assays of the collected release media. Prior to release solution testing, the minimum inhibitory concentration (MIC) and minimum bactericidal concentration (MBC) of gentamicin sulfate against the test strains were established. Gentamicin sulfate exhibited potent activity against *S. aureus*, with an MIC of 0.72 μg/mL and an MBC of 2.88 μg/mL (**Supplementary Figure S12**), whereas both the MIC and MBC for *P. aeruginosa* were 2.88 μg/mL (**Supplementary Figure S13**). Based on these thresholds and the measured release kinetics, the antibiotic concentrations released from the gated systems on day 90 were predicted to remain well above bactericidal levels for both species. Consistent with this prediction, antibacterial

assays using release solutions collected at designated Bac-MPs trigged time points (Fig. 2g) confirmed that release solutions from all gentamicin sulfate-loaded groups on day 1 achieved complete killing of both *S. aureus* and *P. aeruginosa*. After the initial burst release, the TNT@G group showed no further antibacterial activity at any subsequent time point (Fig. 2h). In contrast, release solutions from the gated systems, collected after Bac-MPs stimulation on days 7, 15, 30, 45, 60, and 90, consistently eradicated nearly 100% of both bacterial strains (Fig. 2h and **Supplementary Figure S14**). By day 180, enzyme-triggered release solutions no longer produced detectable bacterial killing, and this loss of activity coincided with complete depletion of the drug reservoir (**Supplementary Figure S8** and **Supplementary Figure S14**).

Furthermore, transcriptomic sequencing was performed to characterize the antibacterial mechanism of TNT-PPN@G against *S. aureus*. Exposure to TNT-PPN@G for 2 h induced significant differential expression of 246 genes, including 135 upregulated and 111 downregulated genes (**Supplementary Figure S15**). Gene Ontology (GO) analysis revealed significant enrichment in pathways associated with cellular metabolism, amino acid activation, tRNA aminoacylation, and RNA binding, indicating disruption of core bacterial metabolic and protein synthesis processes (Fig. 2i). This mechanism was consistent with that of gentamicin sulfate[33]. These findings demonstrated that TNT-PPN@G could release gentamicin sulfate and retains its mechanism of action, exerting antibacterial effects not only via membrane damage but also through comprehensive disruption of bacterial translation and metabolic function.

3.3 *In Vitro* Cell assay

Cytocompatibility was assessed using human bone marrow mesenchymal stem cells (hBMSCs), the key cell type responsible for periprosthetic bone formation (Fig. 3a). Fluorescence microscopy showed that hBMSCs adhered and spread normally on all substrates and maintained a healthy morphology throughout the 5-day culture period (Fig. 3b). CCK-8 assays revealed a modest reduction in viability on bare TNT and ungated TNT@G surfaces, with relative cell counts of 89.56% and 95.51% on day 1, 81.84% and 94.00% on day 3, and 85.23% and 90.43% on day 5, respectively. This reduction was attributable to the specific morphology of the bilayer TNT[34–36] and the burst release of gentamicin sulfate from TNT@G. Immobilization of PP or PPN gating molecules fully restored biocompatibility to levels comparable to that on pristine Ti. Specifically, compared to Ti, the cell viability on TNT-PP@G and TNT-PPN@G was 1.01-fold and 1.02-fold on day 1, 1.04-fold and 1.10-fold on day 3, and 1.08-fold and 1.00-fold on day 5, respectively (Fig. 3c). This finding indicated that the polymer gate layer effectively mitigated the mild cytotoxicity associated with both the bare nanotube surfaces and the burst release of gentamicin sulfate.

Importantly, surface functionalization did not compromise the osteogenic potential of the surfaces. Quantitative real-time reverse transcription polymerase chain reaction (qRT-PCR) analysis of hBMSCs after 7 and 14 days of culture showed comparable expression of ALP, COL I, and OPN across all experimental groups. Notably, RUNX 2 expression was higher in TNT-PPN@G than in the control groups

(**Supplementary Figure S16**). In the alkaline phosphatase (ALP) activity assay, hBMSCs cultured on all TNT-based substrates exhibited higher ALP activity than those cultured on pristine Ti after 14 days, indicating that the TNT structure enhanced osteogenic differentiation. Moreover, compared with TNT@G, which served as the burst-release control, TNT-PP@G and TNT-PPN@G showed increased ALP activity, reaching 1.14-fold and 1.15-fold that of TNT@G, respectively (**Supplementary Figure S17** and **Supplementary Figure S18**). Alizarin red staining revealed a similar trend. At 7, 14, and 21 days, calcium nodule deposition on the controlled-release TNT-PP@G and TNT-PPN@G substrates was higher than that on the burst-release TNT@G substrate. In addition, TNT-based substrates significantly promoted calcium nodule deposition compared with pristine Ti (**Supplementary Figure S19** and **Supplementary Figure S20**).

Given the central role of the immune microenvironment in implant integration and infection resolution, we next investigated the response of RAW 264.7 macrophages to the functionalized surfaces (Fig. 3d). The presence of NaB on the gatekeeper molecules exerted a powerful and specific immunomodulatory effect. On TNT-PPN and TNT-PPN@G surfaces, both containing NaB, the expression of pro-inflammatory markers was dramatically suppressed. Specifically, relative to the Ti control, transcript levels of iNOS, TNF-α, and IL-1β were reduced to 0.84-, 0.64-, and 0.49-fold for TNT-PPN, and 0.86-, 0.61-, and 0.41-fold for TNT-PPN@G, respectively (Fig. 3e). Concomitantly, the expression of the anti-inflammatory cytokine IL-10 was significantly upregulated, increasing by 1.18-fold and 1.24-fold on TNT-PPN and TNT-PPN@G, respectively (Fig. 3e). In contrast, all NaB-free control surfaces, including Ti, TNT, TNT-PP, TNT@G, and TNT-PP@G, elicited negligible changes in the expression of these genes compared to Ti (Fig. 3e), confirming that the observed effect is uniquely attributable to NaB. Flow cytometry analysis of CD206 further revealed a striking increase in M2-polarized cells exclusively on NaB-bearing surfaces. After 3 days of culture, only 1.13% to 1.31% of RAW 264.7 cells were CD206-positive on NaB-free controls. In contrast, the proportion of M2 macrophages surged to 7.76% on TNT-PPN and 8.58% on TNT-PPN@G (Fig. 3f and **Supplementary Figure S21**). These results demonstrated that surface-tethered NaB potently reprogramed macrophages towards a pro-regenerative M2 phenotype, thereby establishing an intrinsically anti-inflammatory local milieu.

3.4 *In vivo* protection against early-stage secondary infection introduced 7 days after implantation

The sequential two-site infection model was employed to evaluate protection against a secondary infection introduced 7 days after initial implant placement, a time point representing the acute period and a high-risk window for delayed infection. The functionalized implant (Test Screw) was first placed into a prepared bone defect. 7 days later, a second implant made of pristine titanium (Infected Screw) was inserted 2.0 mm away from the primary implant to recapitulate an early-stage secondary infection remote from the initial surgical site (Fig. 4a). Inoculation with the Infected Screw alone induced a time-dependent elevation in local Bac-MPs activity, with levels rising progressively from day 1 to day 30 post-infection (**Supplementary Figure S22**). This sustained enzymatic activity confirmed the establishment of

a persistent infection microenvironment and validated the presence of a continuous trigger for the gatekeeper release system.

At 7 days after Infected Screw implantation, corresponding to 14 days after the initial surgery, macroscopic evaluation revealed extensive white purulent secretions and necrotic tissue surrounding the Test Screws in all gentamicin sulfate-free control groups, including Ti, TNT, TNT-PP, and TNT-PPN (Fig. 4b). Strikingly, even the ungated gentamicin sulfate-loaded TNT@G screws exhibited pronounced tissue necrosis (Fig. 4b). This failure was attributable to the rapid burst release of gentamicin sulfate within the first 24 h (Fig. 1i), which left no residual antibiotic to combat the secondary infection introduced on day 7. In contrast, the tissue surrounding TNT-PP@G and TNT-PPN@G implants remained healthy and indistinguishable from uninfected sham controls, demonstrating successful on-demand antibiotic release triggered by the remotely established infection.

Quantitative bacterial recovery assays on both the Test Screws and the adjacent Infected Screws corroborated these macroscopic findings (Fig. 4c and **Supplementary Figure S23**). All gentamicin sulfate-free controls and the ungated TNT@G group exhibited heavy bacterial colonization on both screw surfaces. By contrast, TNT-PP@G and TNT-PPN@G implants achieved nearly 100% bacterial clearance, not only on the Test Screw itself but also on the Infected Screw located 2 mm away. This result demonstrated that enzyme-responsive gentamicin sulfate release from gatekeeper-modified implants generated a sustained antibacterial field potent enough to eradicate an established, spatially separated secondary infection focus.

Histological analysis via hematoxylin and eosin (H&E) staining further supported these functional results (Fig. 4d). The control groups, including Ti, TNT, TNT-PP, and TNT@G, displayed dense inflammatory infiltrates and disrupted tissue architecture around both the Test and Infected Screws, although TNT-PPN showed a modest reduction in inflammatory cell infiltration compared with the other controls. Conversely, TNT-PP@G and TNT-PPN@G groups maintained normal tissue morphology with minimal inflammatory cell infiltration at both implant sites. Compared with the control groups, the inflammatory cell infiltrate percentage in the TNT-PP@G group was reduced to 0.55-, 0.61-, 0.58-, 0.96-, and 0.67-fold, respectively, and in the TNT-PPN@G group it was further reduced to 0.35-, 0.39-, 0.37-, 0.61-, and 0.42-fold. Moreover, TNT-PPN@G achieved a 0.64-fold reduction in inflammatory infiltrate relative to TNT-PP@G (Fig. 4e), indicating that NaB in the gate layer provided additional anti-inflammatory benefit. This conclusion is also supported by the modest attenuation of inflammatory cell infiltration observed in the TNT-PPN group relative to the other controls.

To elucidate the interplay among the test implants, local infection, and macrophage responses, transcriptomic sequencing was performed on tissues from the TNT and TNT-PPN@G groups. At 7 days, the TNT-PPN@G implant induced 15,928 significantly differentially expressed genes, with 4,585 upregulated and 6,640 downregulated relative to TNT (**Supplementary Figure S24**). The overall gene expression pattern regulated by TNT-PPN@G was distinct and of greater magnitude than that of TNT (**Supplementary Figure S25**), and correlation analysis confirmed that the expression patterns between

the two groups were dissimilar ($R^2 > 0.800$) (**Supplementary Figure S26**). Gene Ontology analysis revealed that TNT-PPN@G markedly affected macrophage metabolism, modulating small GTPase-mediated migration, actin cytoskeleton, calcium ion transmembrane transporter activity, mitochondrial respiratory chain complex I, and oxidative phosphorylation, all of which pointed to a reprogramming of macrophage polarization (Fig. 4f). The implant also altered macrophage defense responses, redox status, and cellular behaviors critical for phagocytosis and migration (Fig. 4f). KEGG analysis further demonstrated that TNT-PPN@G significantly reprogrammed macrophage functions by regulating proteasome-dependent degradation pathways, thereby impacting NF-κB signaling, enhancing lysosomal activity and mTOR signaling, and altering the citrate cycle and pyruvate metabolism to shift macrophage polarization (Fig. 4g). A co-expression Venn diagram confirmed that TNT-PPN@G elicited a specific set of gene expression changes not observed with TNT alone (**Supplementary Figure S27**). Overall, these transcriptomic findings demonstrated that the TNT-PPN@G implant achieved rapid bacterial killing and simultaneously induced comprehensive changes in local cellular metabolism, including translation and amino acid metabolism, to alleviate inflammation.

3.5 In vivo protection against late-stage secondary infection introduced 30 days after implantation with a 7-day infection period

We next assessed protection against a late-stage secondary infection using a similar sequential two-site infection model in SD rats. In this model, the functionalized Test Screw was implanted first, and 30 days later an Infected Screw was inserted 2.0 mm away from Test Screw in the pre-inoculated hole with *S. aureus*. Animals were euthanized 7 days after the introduction of the Infected Screw, corresponding to 37 days after the initial implantation (Fig. 5a). Persistent Bac-MPs activity confirmed that an infection microenvironment was still effectively established at this late time-point.

Macroscopic evaluation at day 37 revealed that all gentamicin sulfate-free controls and the ungated TNT@G group exhibited extensive purulent secretions and tissue necrosis, whereas the tissue surrounding TNT-PP@G and TNT-PPN@G implants remained healthy and comparable to uninfected sham controls (Fig. 5b). This result demonstrated that the gatekeeper layers effectively sealed gentamicin sulfate inside the nanotubes during the 30-day infection-free period and that robust antibiotic release was triggered only upon the remote enzymatic challenge. Quantitative bacterial recovery assays confirmed that TNT-PP@G and TNT-PPN@G achieved nearly 100% bacterial clearance on both the Test Screws and the adjacent Infected Screws, while all other groups showed heavy colonization (Fig. 5c and **Supplementary Figure S28**).

Consistent with the antibacterial results, H&E staining revealed markedly fewer inflammatory cells in the connecting segment between the Test and Infected Screws in the TNT-PPN and TNT-PPN@G groups than in Ti, TNT, TNT-PP, TNT@G, and TNT-PP@G groups (Fig. 5d). Quantification of this region showed that the inflammatory cell infiltrate percentage in the TNT-PPN@G group was reduced to 0.45-, 0.38-, 0.41-, 0.56-, and 0.32-fold relative to the Ti, TNT, TNT-PP, TNT-PPN, and TNT@G groups, respectively, and to 0.50-fold relative to TNT-PP@G (Fig. 5e). In line with this, Trap staining showed considerably lower

osteoclast activity in the same connecting segment in the NaB-containing TNT-PPN and TNT-PPN@G groups than in the other groups, in which pronounced osteoclast activity remained, especially when bacteria were not effectively killed (Fig. 5f). Collectively, these results indicate that NaB effectively alleviated local inflammation and suppressed osteoclast activity *in vivo*.

Masson staining revealed evident collagen deposition in the connecting segment between the Test and Infected Screws in all groups (Fig. 5g). Notably, the percentage of new bone area in this segment in the TNT-PPN@G group was 0.29-, 0.26-, 0.29-, 0.20-, and 0.44-fold higher than that in the Ti, TNT, TNT-PP, TNT-PPN, and TNT@G groups, respectively, and was 0.09-fold higher than that in the TNT-PP@G group (Fig. 5h).

We further evaluated osseointegration by methylene blue and basic fuchsin staining. The Test and Infected Screws in TNT-PP@G and TNT-PPN@G groups promoted evident new bone formation, with gradual osteogenesis and irregular cortical bone thickening, particularly in the TNT-PPN@G group (Fig. 5i). Quantitative analysis of bone-implant contact (BIC) showed that Test and Infected Screws in both the TNT-PP@G and TNT-PPN@G groups had significantly greater BIC than those in all other control groups, and no significant difference was observed between TNT-PP@G and TNT-PPN@G. Specifically, in the TNT-PPN@G group, the BIC of the Test Screw was 2.32-, 2.32-, 2.37-, 1.57-, and 2.45-fold that of the Ti, TNT, TNT-PP, TNT-PPN, and TNT@G groups, respectively, and that of the Infected Screw was 1.77-, 1.79-, 1.69-, 1.82-, and 1.90-fold that of the Ti, TNT, TNT-PP, TNT-PPN, and TNT@G groups, respectively (**Supplementary Figure S29**).

Micro-CT analysis further confirmed that TNT-PPN@G screws markedly protected local osteogenesis in the infected specimens (Fig. 5j and **Supplementary Figure S30**). Compared with the Ti, TNT, TNT-PP, TNT-PPN, and TNT@G groups, the BV/TV of the Test Screw in the TNT-PPN@G group was 0.26-, 0.18-, 0.20-, 0.13-, and 0.16-fold higher (Fig. 5k), and the BV/TV of the Infected Screw in the TNT-PPN@G group was 0.15-, 0.09-, 0.17-, 0.08-, and 0.09-fold higher (Fig. 5l). Meanwhile, the BMC of the Test Screw in the TNT-PPN@G group was 1.61-, 1.14-, 0.97-, 0.81-, and 1.14-fold higher (Fig. 5m), and the BMC of the Infected Screw in the TNT-PPN@G group was 0.76-, 0.38-, 0.45-, 0.45-, and 0.41-fold higher (Fig. 5n). Although TNT-PP@G also outperformed the other controls, the BV/TV and BMC of the Test Screw in the TNT-PP@G group remained 0.02-fold and 0.35-fold lower than those of the TNT-PPN@G group, and the BV/TV and BMC of the Infected Screw in the TNT-PP@G group remained 0.04-fold and 0.14-fold lower than those of the TNT-PPN@G group (Fig. 5k to Fig. 5n).

3.6 In vivo protection against late-stage secondary infection introduced 30 days after implantation with a 30-day infection period

We also assessed protection against a late-stage secondary infection using the same sequential two-site infection model in SD rats. In this model, the functionalized Test Screw was implanted first, and 30 days later an Infected Screw was inserted 2.0 mm away from Test Screw in the pre-inoculated hole with *S. aureus*. Animals were euthanized 30 days after the introduction of the Infected Screw, corresponding to 60 days after the initial implantation (Fig. 6a).

Macroscopic evaluation at day 60 revealed that all gentamicin sulfate-free controls and the ungated TNT@G group exhibited extensive purulent secretions and tissue necrosis, whereas the tissue surrounding TNT-PP@G and TNT-PPN@G implants remained healthy and comparable to uninfected sham controls (Fig. 6b). Quantitative bacterial recovery assays also confirmed that TNT-PP@G and TNT-PPN@G achieved nearly 100% bacterial clearance on both the Test Screws and the adjacent Infected Screws, while all other groups showed heavy colonization (Fig. 6c and **Supplementary Figure S31**). These results were verified again that the gatekeeper layers could block gentamicin sulfate in nanotubes effectively and realized the enzyme response after 30 days.

Consistent with the antibacterial results, H&E staining revealed markedly fewer inflammatory cells in the connecting segment between the Test and Infected Screws in the TNT-PPN and TNT-PPN@G groups than in Ti, TNT, TNT-PP, TNT@G, and TNT-PP@G groups (Fig. 6d). Quantification of this region showed that the inflammatory cell infiltrate percentage in the TNT-PPN@G group was reduced to 0.52-, 0.48-, 0.48-, 0.91-, and 0.39-fold relative to the Ti, TNT, TNT-PP, TNT-PPN, and TNT@G groups, respectively, and to 0.70-fold relative to TNT-PP@G (Fig. 6e). These data indicated that NaB provided sustained long-term local anti-inflammatory activity. In line with this, Trap staining showed considerably lower osteoclast activity in the same connecting segment in the NaB-containing TNT-PPN and TNT-PPN@G groups than in the other groups (Fig. 6f). Collectively, these results indicate that NaB could effectively regulate local inflammation, improve the osteogenic environment and regulate the osteogenic process *in vivo*.

Masson staining revealed prominent blue-stained new bone tissue in the connecting segment between the Test and Infected Screws in all groups (Fig. 6g). Notably, the percentage of new bone area in this segment in the TNT-PPN@G group was 0.39-, 0.85-, 0.20-, 0.14-, and 0.20-fold higher than that in the Ti, TNT, TNT-PP, TNT-PPN, and TNT@G groups, respectively, and was 0.04-fold higher than that in the TNT-PP@G group (Fig. 6h).

Methylene blue and basic fuchsin staining revealed that within 30 days after S. aureus challenge, obvious bone erosion appeared near the Infected Screws in the Ti, TNT, TNT-PP, TNT-PPN, and TNT@G groups, and also it could be observed that the Infected Screws in the Ti, TNT, TNT-PP, TNT-PPN, TNT@G and TNT-PP@G groups had obvious bone loosening at the nail cap, while the Infected Screw in the TNT-PPN@G group was closely combined with local bone tissue.. The Test and Infected Screws in TNT-PP@G and TNT-PPN@G groups promoted evident new bone formation, with gradual osteogenesis and irregular cortical bone thickening, particularly in the TNT-PPN@G group (Fig. 6i). Quantitative analysis of BIC also showed that Test and Infected Screws in both the TNT-PP@G and TNT-PPN@G groups had significantly greater BIC than those in all other control groups, and no significant difference was observed between TNT-PP@G and TNT-PPN@G. Specifically, in the TNT-PPN@G group, the BIC of the Test Screw was 1.39-,1.29-, 1.35-, 1.08-, and 1.20-fold that of the Ti, TNT, TNT-PP, TNT-PPN, and TNT@G groups, respectively, and that of the Infected Screw was 1.64-, 1.73-, 1.75-, 1.73-, and 1.93-fold that of the Ti, TNT, TNT-PP, TNT-PPN, and TNT@G groups, respectively (**Supplementary Figure S32**).

Micro-CT analysis further confirmed that TNT-PPN@G screws markedly protected local osteogenesis in long-term infection model (Fig. 6j and **Supplementary Figure S33**). Compared with the Ti, TNT, TNT-PP, TNT-PPN, and TNT@G groups, the BV/TV of the Test Screw in the TNT-PPN@G group was 0.20-, 0.19-, 0.21-, 0.13-, and 0.20-fold higher (Fig. 6k), and the BV/TV of the Infected Screw in the TNT-PPN@G group was 0.19-, 0.19-, 0.21-, 0.16-, and 0.19-fold higher (Fig. 6l). Meanwhile, the BMC of the Test Screw in the TNT-PPN@G group was 0.83-, 0.74-, 0.66-, 0.29-, and 0.41-fold higher (Fig. 6m), and the BMC of the Infected Screw in the TNT-PPN@G group was 0.14-, 0.13-, 0.17-, 0.07-, and 0.14-fold higher (Fig. 6n). Although TNT-PP@G also outperformed the other controls, the BV/TV and BMC of the Test Screw in the TNT-PP@G group remained 0.06-fold and 0.04-fold lower than those of the TNT-PPN@G group, and the BV/TV and BMC of the Infected Screw in the TNT-PP@G group remained 0.07-fold and 0.04-fold lower than those of the TNT-PPN@G group (Fig. 6k to Fig. 6n).

Collectively, these results revealed that TNT-PPN@G not only resolved sudden infections occurring long time after implant placement but also promoted robust long-term osteogenesis following infection control, with NaB playing a critical role in controlling local inflammation throughout the extended repair period.

3.7 *In vivo* osseointegration in a non-infection model

To determine whether the Test Screws would adversely affect bone healing in the absence of infection, a 90-day non-infection bone defect model was established (Fig. 7a). Gross anatomical inspection at 90 days revealed well-healed bone in all groups, with no signs of local infection (Fig. 7b).

Methylene blue and basic fuchsin staining of samples harvested at 90 days showed that dense bone tissue had formed around the screws in all groups. The screw surfaces were completely covered, and irregular new bone formation was observed in the cortical bone region (Fig. 7c). Notably, bone formation around Ti was less than that around the TNT-based groups. Quantification of BIC further showed the similar trend, that BIC values for TNT, TNT-PP, TNT-PPN, TNT@G, TNT-PP@G, and TNT-PPN@G were 0.33-, 0.34-, 0.53-, 0.38-, 0.35-, and 0.50-fold higher than that of Ti, respectively, with no significant differences among the TNT-based groups(Fig. 7d).

Micro-CT analysis showed that periprosthetic bone formation around TNT-PP@G and TNT-PPN@G implants was comparable to that in the other groups, irrespective of gentamicin sulfate incorporation (Fig. 7e). All groups also had similar BV/TV values (Fig. 7f), compared with Ti, BV/TV was 0.98-, 0.95-, 0.98-, 1.10-, 0.98-, and 1.02-fold in TNT, TNT-PP, TNT-PPN, TNT@G, TNT-PP@G, and TNT-PPN@G. Notably, compared with Ti, BMC was 1.08-, 1.06-, 1.11-, 1.10-, 1.11-, and 1.12-fold in TNT, TNT-PP, TNT-PPN, TNT@G, TNT-PP@G, and TNT-PPN@G (Fig. 7g), respectively, but did not differ among these groups. Because bone volume fraction, BV/TV, reflected the proportion of bone volume while bone mineral content, BMC, reflected the degree of mineralization within bone, the increase in BMC without a corresponding increase in BV/TV in the TNT-based groups suggested that the TNT structure promoted mineralization of newly formed bone. This finding was consistent with the alkaline phosphatase

(**Supplementary Figure S17** and **Supplementary Figure S18**) and alizarin red (**Supplementary Figure S19** and **Supplementary Figure S20**) results and with the methylene blue and basic fuchsin staining (Fig. 7c), indicating that under non-infected conditions the TNT structure promotes osseointegration.

To assess systemic biocompatibility, sections of major organs were subjected to H&E staining, and no pathological changes were detected in any of the groups (**Supplementary Figure S34**). Collectively, these results indicated that even in the absence of infection, the long-term retention of gentamicin sulfate within the TNT-PP@G and TNT-PPN@G implants did not compromise normal osseointegration.

4.Discussion

Implant-associated osteomyelitis (IAO) remains a devastating complication of orthopedic surgery, and current antibacterial implant strategies are constrained by two fundamental limitations, namely insufficient temporal coverage of the infection risk window and the inability to achieve on-demand antibacterial action without compromising normal osseointegration. In this study, we reported a multifunctional titanium implant surface that addressed both challenges through a rationally designed bilayer titanium dioxide nanotube (TNT) architecture gated by a bacterial metalloproteinase (Bac-MPs)-responsive Pep-PEG_{4000}-NaB conjugate (TNT-PPN@G). This system achieved precise, on-demand antibiotic release spanning the entire subacute infection period while simultaneously suppressing inflammation and promoting bone integration.

A defining feature of our system was the bilayer TNT structure, which distinguished it from conventional single-layer nanotube platforms. The narrow upper layer and wider lower layer collectively provided a substantially larger drug reservoir capacity while maintaining superior mechanical integrity compared with single-layer TNT, as evidenced by higher exfoliation forces (**Supplementary Figure S5**). This structural innovation was critical because it resolved a longstanding tension in nanotube-based drug delivery. Wider nanotubes improved drug loading but compromised mechanical stability[10,37], whereas narrower tubes were mechanically robust but offered limited payload capacity[38,39]. The bilayer architecture captured the advantages of both geometries, enabling sufficient gentamicin sulfate loading to cover the extended subacute risk window without sacrificing the structural durability required for load-bearing orthopedic applications. Moreover, although previous reports indicated that the specific surface morphology of bilayer TNT could induce cytotoxicity[40], a concern also noted in our study, this issue was fully mitigated by the subsequent immobilization of the gatekeeper molecules, as evidenced by the restored cytocompatibility in the gated groups (Fig. 3b and Fig. 3c). In addition, we demonstrated that this TNT structure significantly promoted osteogenesis under non-infected conditions compared with pristine Ti (**Supplementary Figure S16** to **Supplementary Fig. 20**).

The enzyme response performance had the advantages of high efficiency and specificity, which did not depend on the wide range fluctuation of local pH value of tissues and the intervention of external equipment. The core value of enzyme-responsive materials lied in accurate recognition and higher targeting efficiency at the molecular level. The enzyme-responsive gating mechanism represented the

core functional innovation of this platform. By conjugating Pep-PEG_{4000}-NaB to the TNT surface via a Bac-MPs-cleavable peptide linker, we engineered TNT-PPN@G that remained in a quiescent, non-leaching state under physiological conditions but underwent rapid unsealing specifically in the presence of active infection. *In vitro* release data demonstrated that approximately 42.39% of the loaded gentamicin sulfate was released in an initial burst within the first day, after which the remaining drug was effectively retained for over 90 days (Fig. 1i). Enzymatic stimulation triggered consistent, bactericidal levels of drug release at every time point tested (Fig. 2h). This release profile was clinically relevant, as the initial burst provided immediate postoperative infection prophylaxis during the period when the risk of infection was highest and prophylactic antibiotics were routinely administered[41]. The subsequent sustained retention and on-demand release ensured that temporal coverage far exceeded that of existing antibacterial TNT systems, which typically exhausted their payload within days to weeks and were therefore limited to protecting against acute perioperative infection[42]. By spanning the full subacute phase, when delayed and hematogenous infections most frequently occurred, TNT-PPN@G represented a promising strategy to address a clinically important issue in current implant technology.

Notably, the *in vivo* two-site infection model revealed that the gated system responded not only to direct bacterial contact but also to remotely established infection foci 2.0 mm away (Fig. 4b, Fig. 5b, and Fig. 6b). This spatially extended protective effect was particularly significant because clinical periprosthetic infections often originated from distant hematogenous seeding or contiguous spread rather than from direct contamination at the implant surface[43,44]. The sustained local antibacterial field generated by enzyme-triggered release was sufficient to eradicate established infection at both the primary implant and the remote Infected Screw, suggesting that this system could provide broader protection against diverse routes of implant infection than surface-contact-dependent antibacterial coatings.

The inclusion of NaB as a functional component of the gatekeeper molecule added a second layer of therapeutic value that set this design apart from purely antibiotic-based strategies. NaB exerted pleiotropic effects that were mechanistically complementary to the antibacterial function. It suppressed pro-inflammatory cytokine production and reprogrammed macrophages toward an M2-polarized, pro-regenerative phenotype, as confirmed by both *in vitro* gene expression and flow cytometry data and *in vivo* transcriptomic analysis (Fig. 3e Fig. 3f, **Supplementary Figure S21**, Fig. 2i, Fig. 4f, and Fig. 4g). The transcriptomic findings further revealed that TNT-PPN@G modulated macrophage metabolic pathways, including oxidative phosphorylation, mTOR signaling, and proteasome-dependent degradation, providing mechanistic insight into how NaB reshaped the local immune microenvironment (Fig. 4f and Fig. 4g). This immunomodulatory capacity was clinically important because excessive inflammation not only damaged periprosthetic tissue but also impaired osteoblast function and promoted osteoclast-mediated bone resorption, all of which contributed to implant loosening[45].

Beyond its anti-inflammatory role, NaB directly enhanced osseointegration through multiple mechanisms. The *in vivo* data demonstrated that NaB-containing groups exhibited increased new bone

formation, higher bone-implant contact, and improved bone microarchitecture (BV/TV and BMC) compared with NaB-free controls, while Trap staining confirmed reduced osteoclast activity (Fig. 5f and Fig. 6f). These findings were consistent with the known ability of NaB to promote osteoblast differentiation via Wnt/β-catenin signaling and RUNX 2 upregulation and to suppress osteoclastogenesis[30,46]. The triple synergy of bacterial eradication, inflammatory resolution, and osteogenic stimulation enabled TNT-PPN@G to achieve robust osseointegration even under infectious conditions, a feat that conventional antibiotic-loaded implants could not accomplish, as they addressed only the infectious component while leaving inflammation and impaired bone healing unmanaged.

The three sequential *in vivo* infection models collectively established a comprehensive efficacy profile across the temporal spectrum of implant-associated infection. The early-stage secondary infection model (7 + 7 days) validated the on-demand release mechanism and its ability to clear acute secondary infection (Fig. 4). The late-stage secondary infection model with a 7-day infection period (30 + 7 days) confirmed that the gatekeeper structure preserved its function after 30 days of *in vivo* residence, demonstrating long-term drug stability and retained responsiveness, a property essential for protecting against late subacute infections (Fig. 5). The late-stage secondary infection model with a 30-day infection period (30 + 30 days) revealed that successful infection control translated to sustained bone repair and inflammatory homeostasis over an extended period, with no evidence of recurrent infection or chronic inflammatory sequelae (Fig. 6). This progressive validation strategy strengthened the clinical relevance of the findings, as it mirrored the natural history of periprosthetic infection from acute onset through chronic bone destruction[47,48]. Furthermore, in the non-infection model, the TNT-PPN@G implant exhibited no adverse effect on osseointegration, confirming its suitability for use under non-infectious conditions as well (Fig. 7).

In summary, TNT-PPN@G represented an advance in antibacterial implant design. By combining a mechanically robust, high-capacity drug reservoir with intelligent, infection-triggered release and intrinsic immunomodulatory and osteogenic properties, this platform addressed the dual challenges of temporal coverage and the antibacterial-osseointegration trade-off that had limited previous approaches. The demonstration of efficacy across early, delayed, and long-term infection models, together with favorable biocompatibility profiles, positioned this technology as a promising strategy for reducing the burden of implant-associated osteomyelitis and improving outcomes in orthopedic implant surgery.

Declarations

Supporting Information

Supporting Information is available from the Wiley Online Library or from the author.

Conflict of Interest

The authors declare no conflict of interest.

Author Contributions

WTZ: Conceptualization, Methodology, Software, Formal analysis, Writing-Original Draft. ZYH: Methodology, Software, Formal analysis, Writing-Review & Editing. XLP: Methodology, Software, Formal analysis, Writing-Review & Editing. HZ: Software, Validation, Visualization, Project administration. ZYG: Methodology, Investigation, Visualization. RZ: Validation, Investigation, Data Curation. MZ: Methodology, Investigation, Data Curation, Project administration. ZLD: Formal analysis, Resources, Data Curation, Supervision. YLR: Conceptualization, Resources, Supervision. LC: Conceptualization, Resources, Writing-Review & Editing. LW: Conceptualization, Resources, Writing-Review & Editing. WTZ, ZYH and XLP contributed equally to this article as co-first authors.

Acknowledgements

This work was supported by grants from National Key R&D Program of China (2023YFB3809901), Guizhou Provincial Basic Research Program (Natural Science) (Qiankehe Foundation ZD 2025-014), Guizhou Province Health and Wellness High-Quality Development Medical Research (2024GZYXKYJJXM0042), Chronic Disease Management Research Project of National Health Commission Capacity Building and Continuing Education Center (GWJJMB202510025059), Talent Fund of Guizhou Provincial People's Hospital (Institute Talent Program 2024-29), and 2026 Provincial Science and Technology Support Program for Agriculture and Social Development (General Project) (Qiankehe Support 2025 General 340), the National Natural Science Foundation of China (82604826, 82604749, 52571269), the Natural Science Foundation of Chongqing (2024NSCQ-MSX0352).

Data Availability Statement

The data that support the findings of this study are available from the cor-responding author upon reasonable request.

References

1. Geetha M, Singh AK, Asokamani R, Gogia AK (2009) Ti based biomaterials, the ultimate choice for orthopaedic implants – A review. Prog Mater Sci 54:397–425. https://doi.org/https://doi.org/10.1016/j.pmatsci.2008.06.004
2. Arciola CR, Campoccia D, Montanaro L (2018) Implant infections: adhesion, biofilm formation and immune evasion. Nat Rev Microbiol 16:397–409. https://doi.org/10.1038/s41579-018-0019-y
3. Masters EA et al (2019) Evolving concepts in bone infection: redefining biofilm, acute vs. chronic osteomyelitis, the immune proteome and local antibiotic therapy. Bone Res 7:20.

https://doi.org/10.1038/s41413-019-0061-z

4. Darouiche RO (2004) Treatment of infections associated with surgical implants. N Engl J Med 350:1422–1429. https://doi.org/10.1056/NEJMra035415
5. Cook GE et al (2015) Infection in Orthopaedics. J Orthop Trauma 29(12):19–23. https://doi.org/10.1097/bot.0000000000000461
6. Colston J, Atkins B (2018) Bone and joint infection. Clin Med (Lond) 18:150–154. https://doi.org/10.7861/clinmedicine.18-2-150
7. Moriarty TF et al (2022) Fracture-related infection. Nat Rev Dis Primers 8:67. https://doi.org/10.1038/s41572-022-00396-0
8. Kapadia BH et al (2016) Periprosthetic joint infection. Lancet 387:386–394. https://doi.org/10.1016/s0140-6736(14)61798-0
9. Jahanmard F et al (2020) Bactericidal coating to prevent early and delayed implant-related infections. J Control Release 326:38–52. https://doi.org/10.1016/j.jconrel.2020.06.014
10. Zhang Y, Zhang L, Li B, Han Y (2017) Enhancement in Sustained Release of Antimicrobial Peptide from Dual-Diameter-Structured TiO(2) Nanotubes for Long-Lasting Antibacterial Activity and Cytocompatibility. ACS Appl Mater Interfaces 9:9449–9461. https://doi.org/10.1021/acsami.7b00322
11. Niu X, Sun L, Zhang X, Sun Y, Wang J (2020) Fabrication and antibacterial properties of cefuroxime-loaded TiO(2) nanotubes. Appl Microbiol Biotechnol 104:2947–2955. https://doi.org/10.1007/s00253-020-10446-w
12. Shaygani H et al (2023) Novel bilayer coating on gentamicin-loaded titanium nanotube for orthopedic implants applications. Int J Pharm 636:122764. https://doi.org/10.1016/j.ijpharm.2023.122764
13. Wassif RK, Elkayal M, Shamma RN, Elkheshen SA (2021) Recent advances in the local antibiotics delivery systems for management of osteomyelitis. Drug Deliv 28:2392–2414. https://doi.org/10.1080/10717544.2021.1998246
14. Zhou H et al (2025) Efficacy of pH-Responsive Surface Functionalized Titanium Screws in Treating Implant-associated S. aureus Osteomyelitis with Biofilms Formation. Adv Healthc Mater 14:e2403261. https://doi.org/10.1002/adhm.202403261
15. Wang B et al (2022) Dual-functional strontium titanate nanotubes designed based on fusion peptides simultaneously enhancing anti-infection and osseointegration. Biomater Adv 133:112650. https://doi.org/10.1016/j.msec.2022.112650
16. Kavanagh N et al (2018) Staphylococcal Osteomyelitis: Disease Progression, Treatment Challenges, and Future Directions. Clin Microbiol Rev 31. https://doi.org/10.1128/cmr.00084-17
17. Piñera-Avellaneda D et al (2024) Gallium and silver-doped titanium surfaces provide enhanced osteogenesis, reduce bone resorption and prevent bacterial infection in co-culture. Acta Biomater 180:154–170. https://doi.org/10.1016/j.actbio.2024.04.019

18. Ren Y et al (2023) Epidemiological updates of post-traumatic related limb osteomyelitis in china: a 10 years multicentre cohort study. Int J Surg 109:2721–2731. https://doi.org/10.1097/js9.0000000000000502
19. Visse R, Nagase H (2003) Matrix metalloproteinases and tissue inhibitors of metalloproteinases: structure, function, and biochemistry. Circ Res 92:827–839. https://doi.org/10.1161/01.Res.0000070112.80711.3d
20. Potempa J, Banbula A, Travis J (2000) Role of bacterial proteinases in matrix destruction and modulation of host responses. Periodontol 2000 24:153–192. https://doi.org/10.1034/j.1600-0757.2000.2240108.x
21. Zhong R et al (2026) Dual-Anchored Clickable Peptide via SPAAC for Gelatinase-Responsive Antibacterial and Osteogenic Functions on Titanium Implants. Adv Sci (Weinh) 13, e20154 https://doi.org/10.1002/advs.202520154
22. Li LL, Qi GB, Yu F, Liu SJ, Wang H (2015) An adaptive biointerface from self-assembled functional peptides for tissue engineering. Adv Mater 27:3181–3188. https://doi.org/10.1002/adma.201500658
23. Anderson CF, Cui H (2017) Protease-Sensitive Nanomaterials for Cancer Therapeutics and Imaging. Ind Eng Chem Res 56:5761–5777. https://doi.org/10.1021/acs.iecr.7b00990
24. Kraehenbuehl TP et al (2008) Three-dimensional extracellular matrix-directed cardioprogenitor differentiation: systematic modulation of a synthetic cell-responsive PEG-hydrogel. Biomaterials 29:2757–2766. https://doi.org/10.1016/j.biomaterials.2008.03.016
25. D'Souza A, A., Shegokar R (2016) Polyethylene glycol (PEG): a versatile polymer for pharmaceutical applications. Expert Opin Drug Deliv 13:1257–1275. https://doi.org/10.1080/17425247.2016.1182485
26. Liu S et al (2021) Gingipain-Responsive Thermosensitive Hydrogel Loaded with SDF-1 Facilitates In Situ Periodontal Tissue Regeneration. ACS Appl Mater Interfaces 13:36880–36893. https://doi.org/10.1021/acsami.1c08855
27. Ressler A et al (2018) Injectable chitosan-hydroxyapatite hydrogels promote the osteogenic differentiation of mesenchymal stem cells. Carbohydr Polym 197:469–477. https://doi.org/10.1016/j.carbpol.2018.06.029
28. Wu L et al (2022) Enhancing effect of sodium butyrate on phosphatidylserine-liposome-induced macrophage polarization. Inflamm Res 71:641–652. https://doi.org/10.1007/s00011-022-01563-5
29. Park JS, Lee EJ, Lee JC, Kim WK, Kim HS (2007) Anti-inflammatory effects of short chain fatty acids in IFN-gamma-stimulated RAW 264.7 murine macrophage cells: involvement of NF-kappaB and ERK signaling pathways. Int Immunopharmacol 7:70–77. https://doi.org/10.1016/j.intimp.2006.08.015
30. Luo QJ et al (2021) Sodium butyrate protects against lipopolysaccharide-induced liver injury partially via the GPR43/ β-arrestin-2/NF-κB network. Gastroenterol Rep (Oxf) 9:154–165. https://doi.org/10.1093/gastro/goaa085

31. Liu J et al (2019) Sodium Butyrate Inhibits the Inflammation of Lipopolysaccharide-Induced Acute Lung Injury in Mice by Regulating the Toll-Like Receptor 4/Nuclear Factor κB Signaling Pathway. J Agric Food Chem 67:1674–1682. https://doi.org/10.1021/acs.jafc.8b06359
32. Vol (2005) F04.15,. ASTM F1044-05
33. Hahn FE, Sarre SG (1969) Mechanism of action of gentamicin. J Infect Dis 119:364–369. https://doi.org/10.1093/infdis/119.4-5.364
34. Hosseinkhani H, Hosseinkhani M, Tian F, Kobayashi H, Tabata Y (2006) Osteogenic differentiation of mesenchymal stem cells in self-assembled peptide-amphiphile nanofibers. Biomaterials 27:4079–4086. https://doi.org/10.1016/j.biomaterials.2006.03.030
35. Dulgar-Tulloch AJ, Bizios R, Siegel RW (2009) Human mesenchymal stem cell adhesion and proliferation in response to ceramic chemistry and nanoscale topography. J Biomed Mater Res A 90:586–594. https://doi.org/10.1002/jbm.a.32116
36. Lavenus S et al (2011) Adhesion and osteogenic differentiation of human mesenchymal stem cells on titanium nanopores. Eur Cell Mater 22, 84–96; discussion 96 https://doi.org/10.22203/ecm.v022a07
37. Xiong F-Q et al (2014) Fabrication of multilayered TiO2 nanotube arrays and separable nanotube segments. J Mater Chem A 2:4510–4513. https://doi.org/10.1039/c3ta15028c
38. Chen B, Lu K (2011) Hierarchically Branched Titania Nanotubes with Tailored Diameters and Branch Numbers. Langmuir 28:2937–2943. https://doi.org/10.1021/la204154h
39. Brammer KS et al (2009) Improved bone-forming functionality on diameter-controlled TiO2 nanotube surface. Acta Biomater 5:3215–3223. https://doi.org/https://doi.org/ 10.1016/j.actbio.2009.05.008
40. Michalkova H et al (2020) Complex cytotoxicity mechanism of bundles formed from self-organised 1-D anodic TiO(2) nanotubes layers. J Hazard Mater 388:122054. https://doi.org/10.1016/j.jhazmat.2020.122054
41. Wei J, Tong K, Wang H, Wen Y, Chen L, Dosage (2022) Efficacy, and Safety of Intra-articular Vancomycin for Prophylaxis of Periprosthetic Joint Infection Caused by Methicillin-Resistant Staphylococcus aureus after Total Knee Arthroplasty in a Rat Model. Antimicrob Agents Chemother 66:e0164121. https://doi.org/10.1128/aac.01641-21
42. Riester O, Borgolte M, Csuk R, Deigner HP (2020) Challenges in Bone Tissue Regeneration: Stem Cell Therapy, Biofunctionality and Antimicrobial Properties of Novel Materials and Its Evolution. Int J Mol Sci 22. https://doi.org/10.3390/ijms22010192
43. Patel R, Periprosthetic Joint Infection (2023) N Engl J Med 388:251–262. https://doi.org/10.1056/NEJMra2203477
44. Nelson SB, Pinkney JA, Chen AF, Tande AJ (2023) Periprosthetic Joint Infection: Current Clinical Challenges. Clin Infect Dis 77:e34–e45. https://doi.org/10.1093/cid/ciad360
45. Thomas MV, Puleo DA (2011) Infection, inflammation, and bone regeneration: a paradoxical relationship. J Dent Res 90:1052–1061. https://doi.org/10.1177/0022034510393967

46. Liu M et al (2025) Sodium butyrate regulates macrophage polarization by TGR5/β-arrestin2 in vitro. Mol Med 31:31. https://doi.org/10.1186/s10020-025-01096-7
47. Grayson WL et al (2015) Stromal cells and stem cells in clinical bone regeneration. Nat Rev Endocrinol 11:140–150. https://doi.org/10.1038/nrendo.2014.234
48. Minear S et al (2010) Wnt proteins promote bone regeneration. Sci Transl Med 2:29ra30. https://doi.org/10.1126/scitranslmed.3000231

Figures

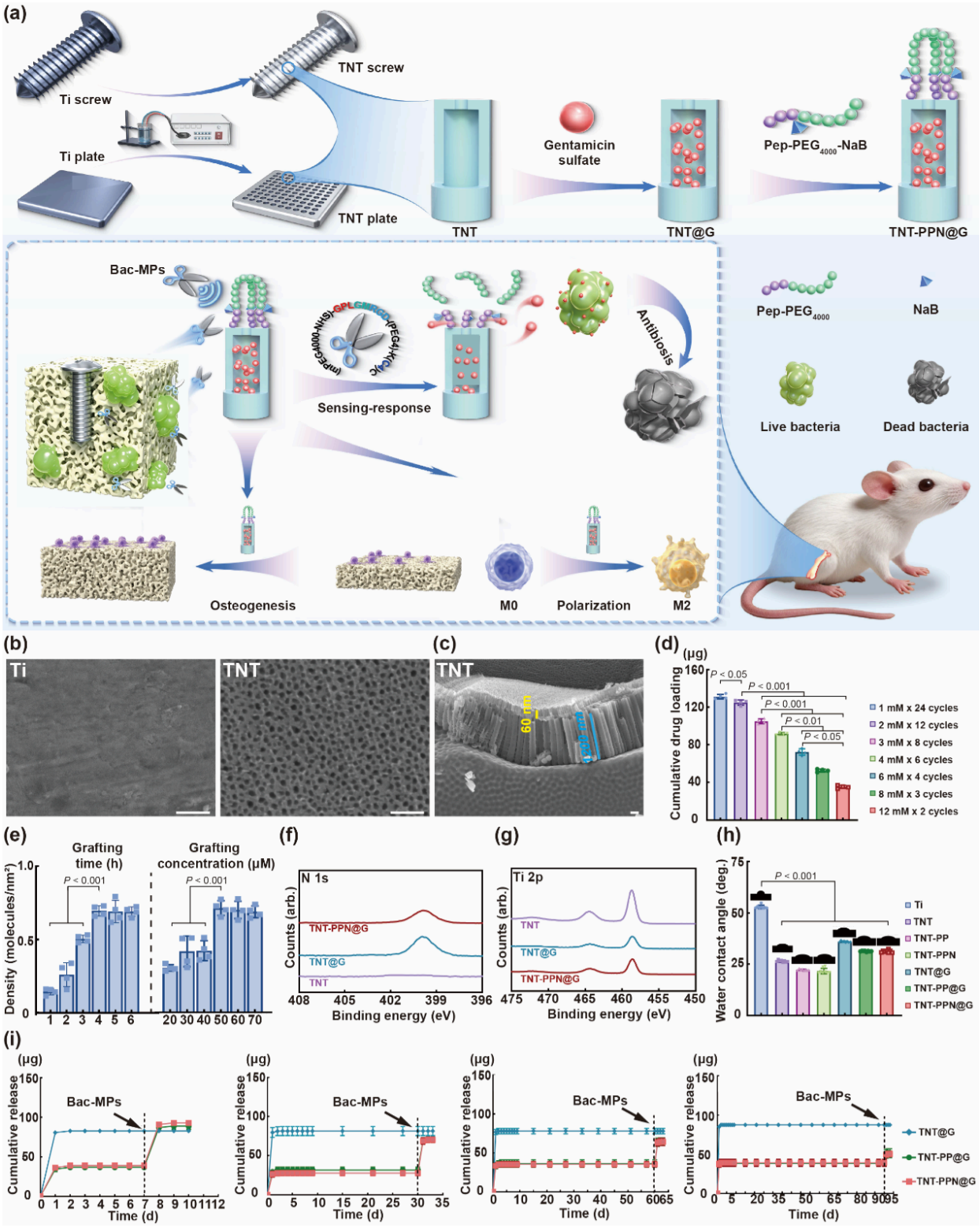

Figure 1

Characterization of gentamicin sulfate-loaded TNT-based implant. (a) Schematic illustration of the preparation process and the responsive antibacterial mechanism of the gentamicin sulfate-loaded TNT-based implant (TNT-PPN@G). (b) SEM images of pristine Ti and the TNT array surface. The scale bar was 100 nm. (c) Cross-sectional SEM image of the TNT arrays. The scale bar was 100 nm. (d) Cumulative gentamicin sulfate loading in TNT arrays prepared with varying drug concentrations and

numbers of loading cycles (n = 4). For each group, the product of the drug concentration and the cycle number was kept constant, such that the total amount of drug applied to each sample was equivalent. (e) Grafting density of PPN gating molecules as a function of grafting time (PPN concentration fixed at 50 μM) and PPN concentration in the grafting solution (grafting time fixed at 4 h) (n = 4). (f) High-resolution XPS N 1s spectra of the indicated samples. (g) High-resolution XPS Ti 2p spectra of the indicated samples. (h) Water contact angle images and quantification for the indicated samples (n = 8). (i) *In vitro* gentamicin sulfate release profile from indicated samples (n = 4). Bac-MPs (5 μg/mL) were introduced on days 7, 30, 60, and 90, respectively.

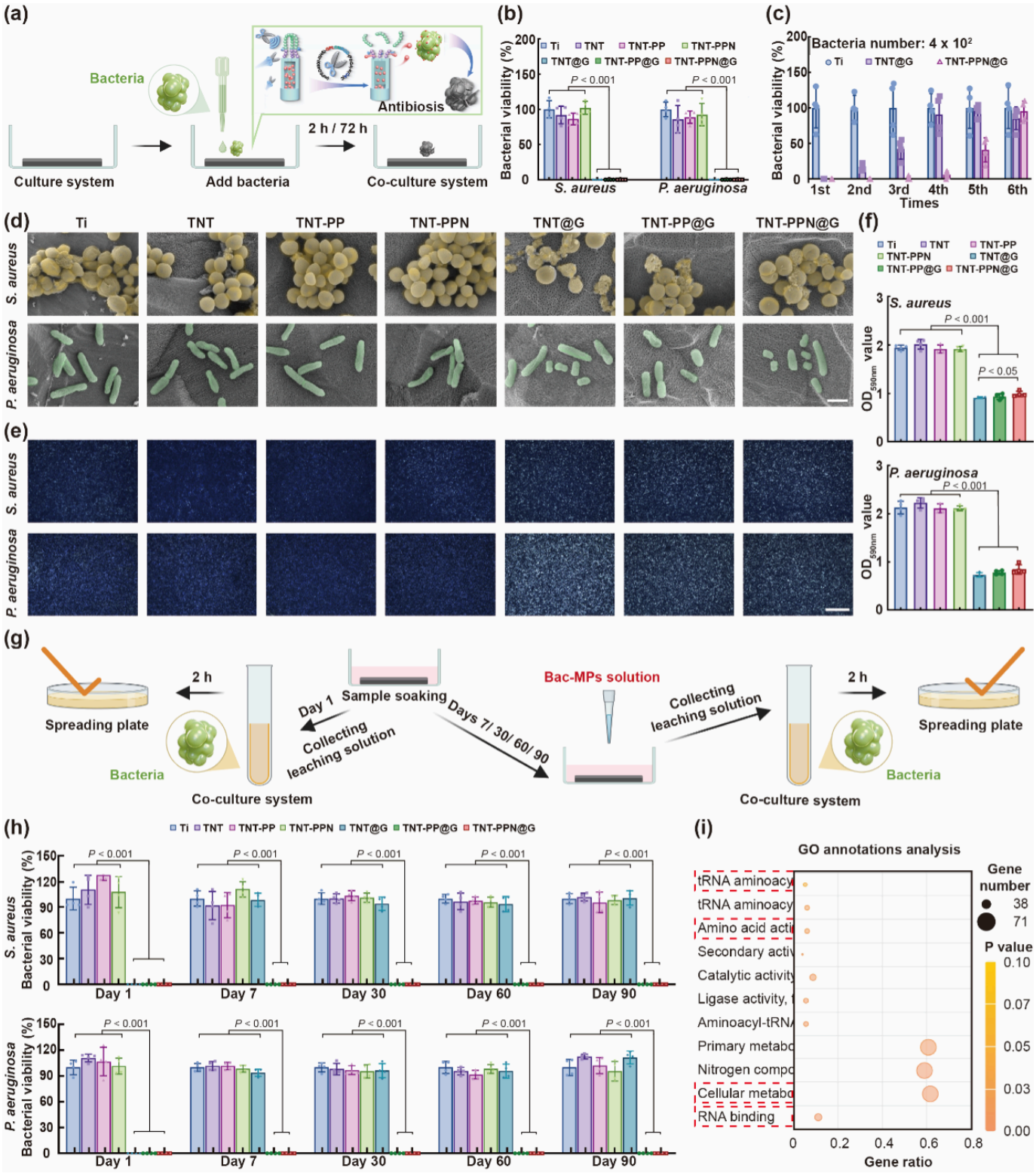

Figure 2

***In vitro* antibacterial activity of gentamicin sulfate-loaded TNT-based implant.** (a) Schematic illustration of the antibacterial assay, in which bacteria were co-cultured with TNT-PPN@G. (b) Bacterial viability after co-culture with the indicated samples (n = 4). (c) Results of the cyclic antibacterial assay with the indicated samples (n = 4). In the cyclic assay, 400 bacteria were seeded per cycle. (d) SEM images of bacteria co-cultured with the indicated samples. *S.aureus* were pseudocolored in yellow, and *P.*

*aeruginosa*were pseudocolored in green. The scale bar was 1 μm. (e) Qualitative and (f) quantitative analysis of biofilm formation by bacteria co-cultured with the indicated samples (n = 4). The scale bar was 1 mm. (g) Schematic illustration of the antibacterial activity of the release solutions from the indicated samples. (h) Antibacterial activity of the release solutions collected on days 1, 7, 30, 60, and 90 (n = 4). (i) Gene Ontology (GO) enrichment analysis of differentially expressed genes (P < 0.05).

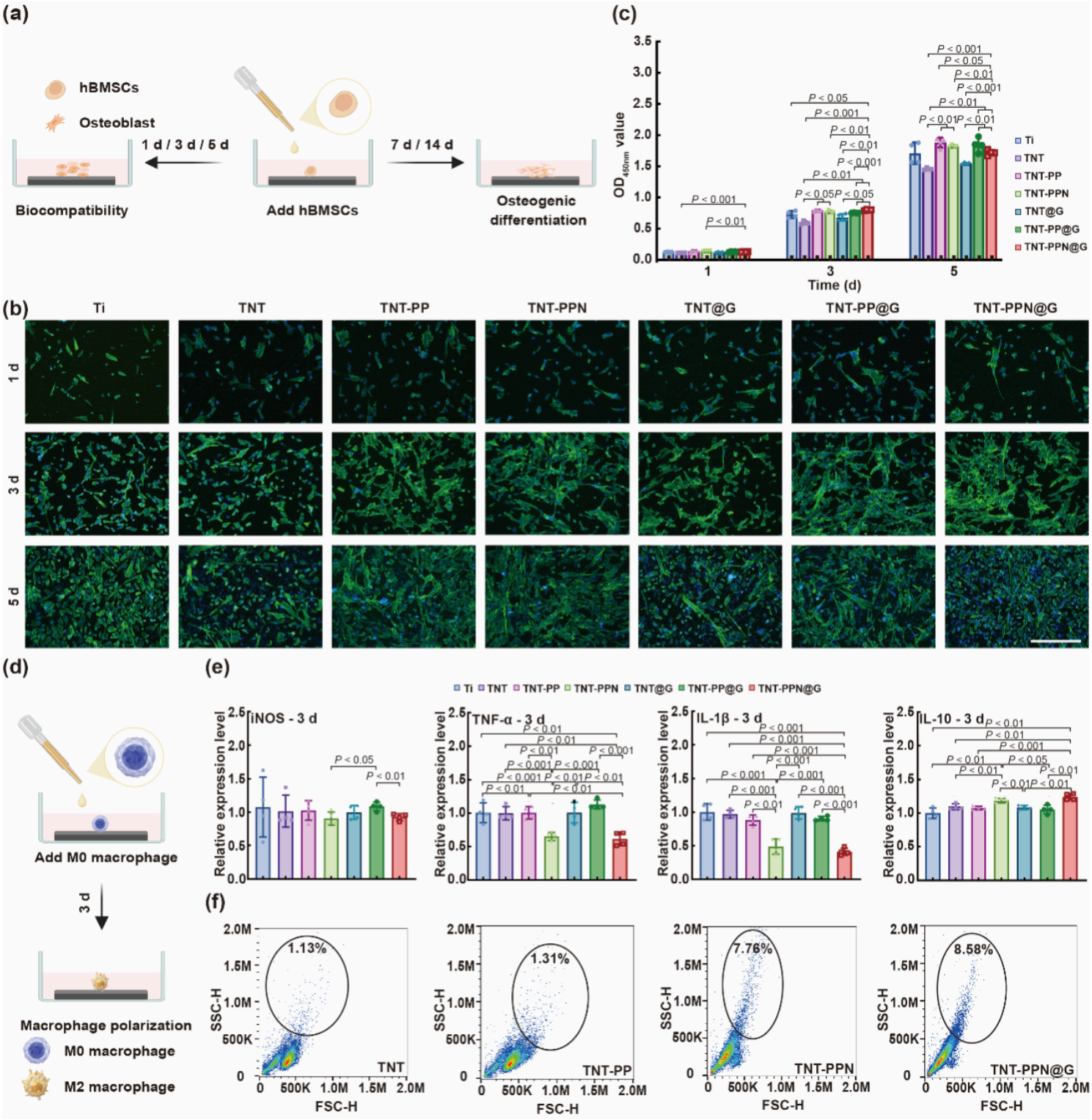

Figure 3

In vitro cell assay of gentamicin sulfate-loaded TNT-based implant. (a) Schematic illustration of hBMSCs co-culture with the indicated samples. (b) Live/dead staining of hBMSCs co-cultured with the indicated samples for 1, 3, and 5 days. The scale bar was 500 μm. (c) CCK-8 assay of hBMSCs co-cultured with the indicated samples for 1, 3, and 5 days (n = 4). (d) Schematic illustration of RAW264.7 co-cultured with the indicated samples. (e) qRT-PCR analysis of inflammatory factor expression (iNOS, TNF-α, IL-1β, and IL-10) after RAW264.7 were co-cultured with the indicated samples for 3 days (n = 4). (f) Flow cytometric analysis of M2-type expression after RAW264.7 cells were co-cultured with the indicated samples for 3 days.

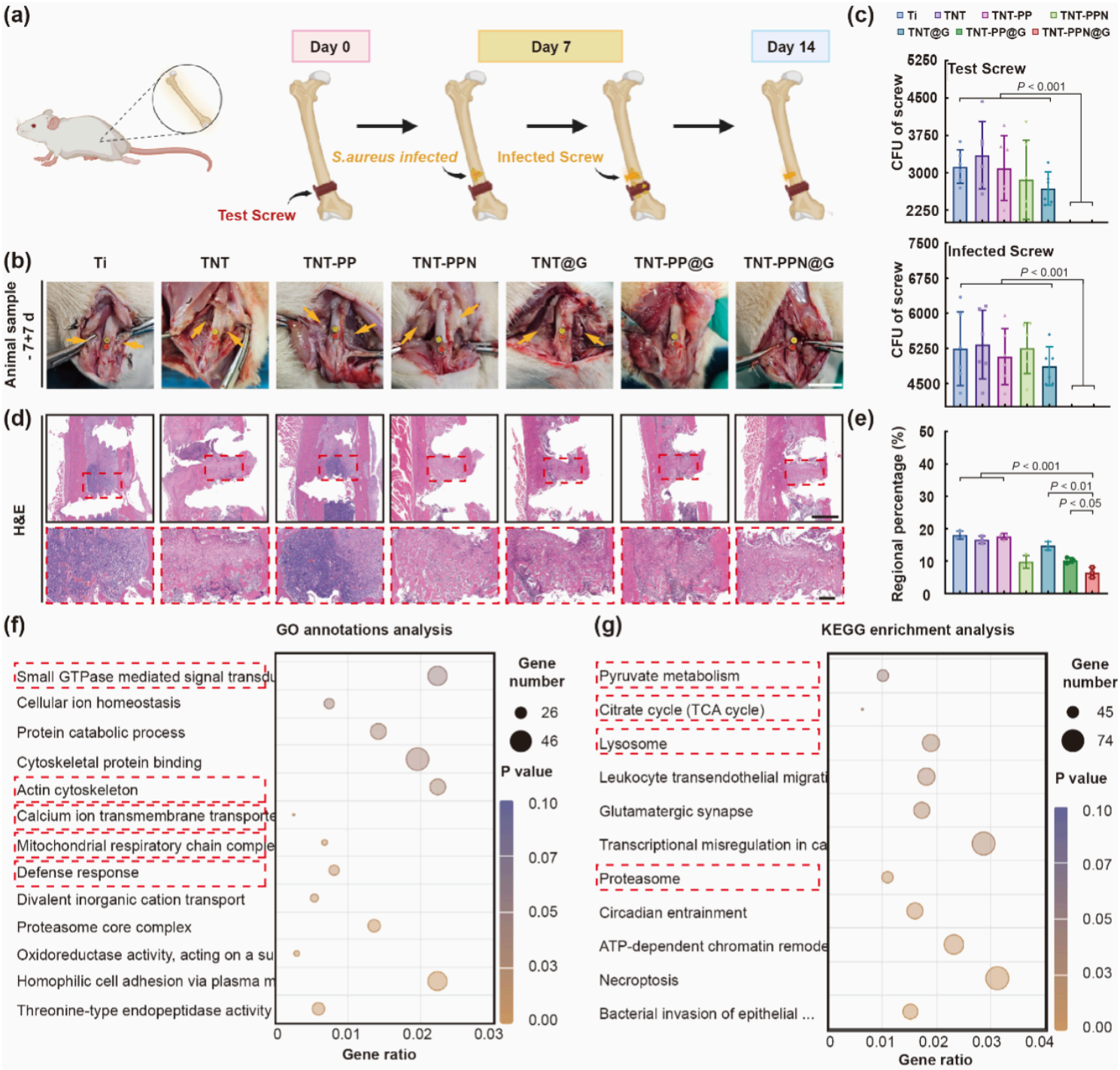

Figure 4

***In vivo* protection against early-stage secondary infection introduced 7 days after implantation with 7-day infection period.** (a) Schematic of the experimental design. 7 days after implantation of the Test Screw into the rat femur, an *S. aureus* infection was established 2 mm proximal to the Test Screw, and a second implant, designated the Infected Screw, was placed. Samples were collected after a further 7 days of infection. (b) Representative photographs taken 7 days after infection induction following 7 days of test implant placement. Scale bar was 2 cm. Yellow circle indicates the Infected Screw, red circle indicates the Test Screw, and yellow arrow indicates the infected area. (c) Bacterial loads on Test Screw and Infected Screw quantified by agar plate assay (n = 6). (d) Representative H&E staining images of decalcified bone sections. Scale bar was 1 mm in the upper panels and 200 μm in the lower panels. (e) Quantification of inflammatory cell area in H&E-stained images (n = 3). (f) Gene Ontology (GO) annotation and (g) Kyoto Encyclopedia of Genes and Genomes (KEGG) enrichment analysis of differentially expressed genes ($P < 0.05$).

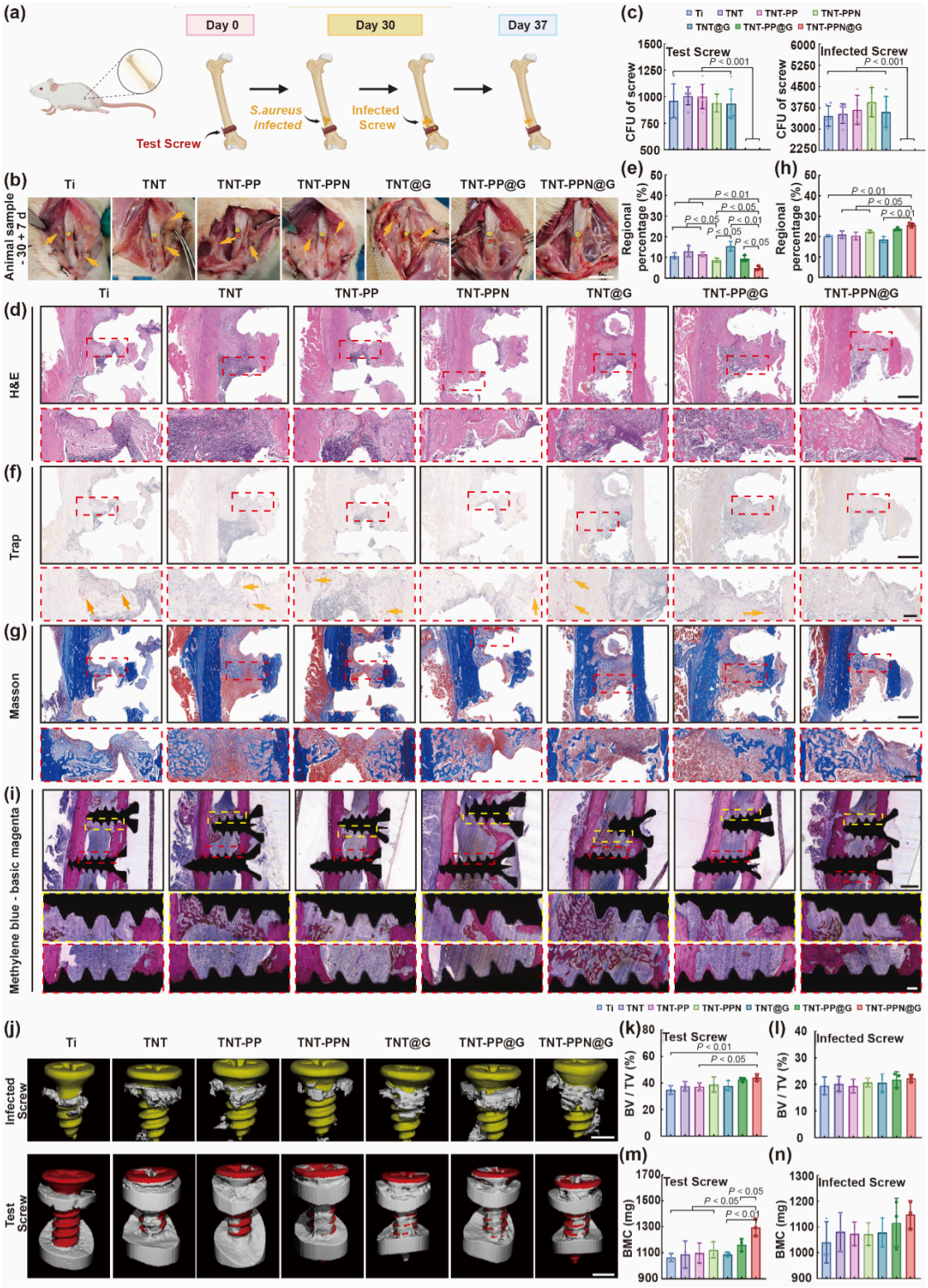

Figure 5

***In vivo* protection against late-stage secondary infection introduced 30 days after implantation with 7-day infection period.** (a) Schematic of the experimental design. 30 days after implantation of the Test Screw into the rat femur, an *S. aureus* infection was established 2 mm proximal to the Test Screw, and a second implant, designated the Infected Screw, was placed. Samples were collected after a further 7 days of infection. (b) Representative photographs taken 7 days after infection induction following 30

days of test implant placement. Scale bar was 2 cm. Yellow circle indicates the Infected Screw, red circle indicates the Test Screw, and yellow arrow indicates the infected area. (c) Bacterial loads on Test Screw and Infected Screw quantified by agar plate assay (n = 6). (d) Representative H&E staining images of decalcified bone sections. Scale bar was 1 mm in the upper panels and 200 μm in the lower panels. (e) Quantification of inflammatory cell area in H&E stained images (n = 3). (f) Representative Trap staining images of decalcified bone section. Scale bar was 1 mm in the upper panels and 200 μm in the lower panels. Yellow arrow indicates the osteoclast active region. (g) Representative Masson staining images of decalcified bone sections. Scale bar was 1 mm in the upper panels and 200 μm in the lower panels. (h) Quantification of collagen deposition in Masson stained images (n = 3). (i) Representative methylene blue-basic magenta staining images of undecalcified bone sections. Scale bar was 1 mm in the upper panels and 200 μm in the lower panels. (j) Micro-CT 3D reconstructed images of the femur around the Test and Infected Screws. The scale bar was 1 mm. The yellow implant indicated the Infected Screw and the red implant indicated the Test Screw. (k) BV/TV of the Test Screw quantified from Micro-CT three-dimensional reconstructed images (n = 3). (l) BV/TV of the Infected Screw quantified from Micro-CT three-dimensional reconstructed images (n = 3). (m) BMC of the Test Screw quantified from Micro-CT three-dimensional reconstructed images (n = 3). (n) BMC of the Infected Screw quantified from Micro-CT three-dimensional reconstructed images (n = 3).

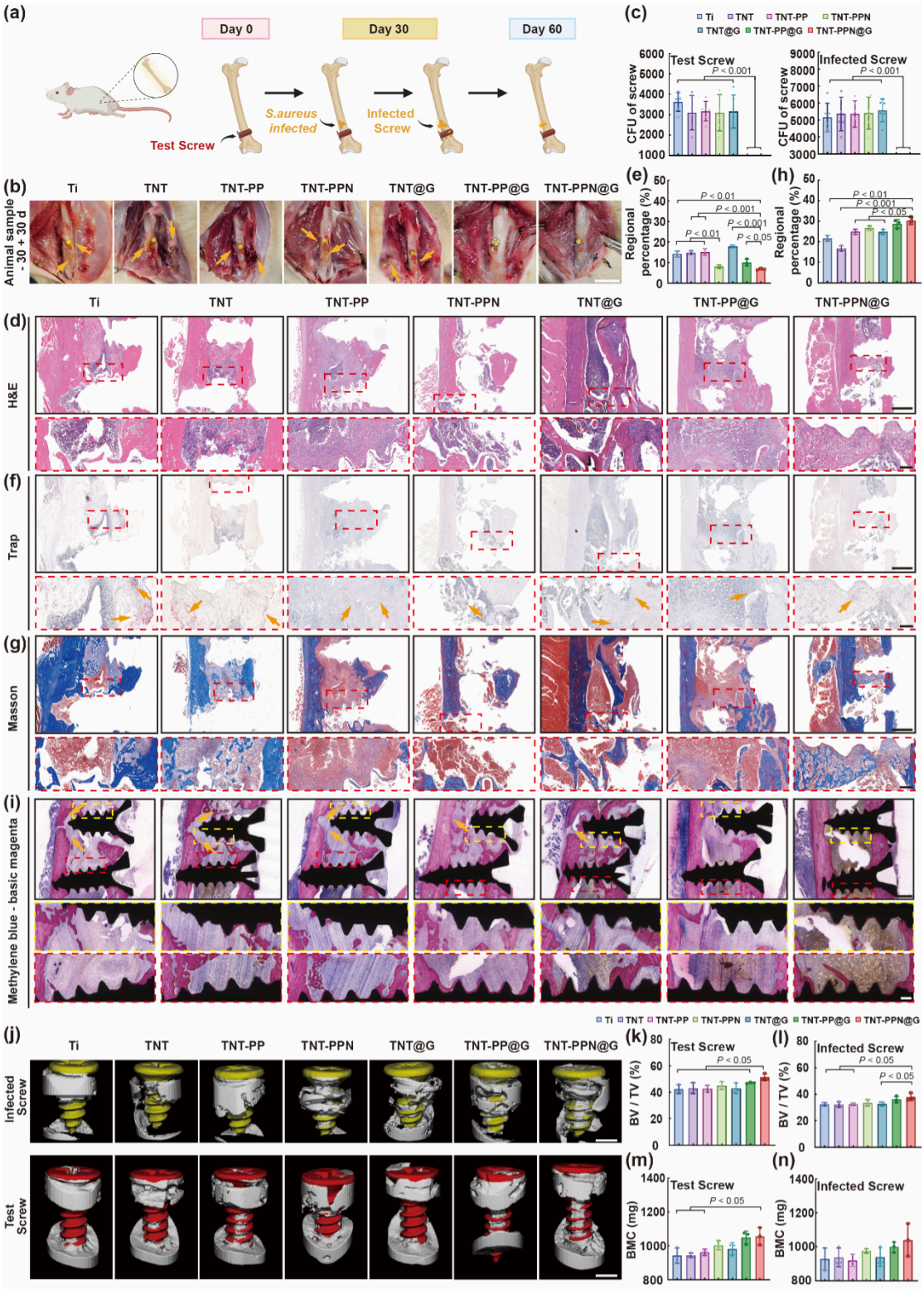

Figure 6

***In vivo* protection against late-stage secondary infection introduced 30 days after implantation with 30-day infection period.** (a) Schematic of the experimental design. 30 days after implantation of the Test Screw into the rat femur, an *S. aureus* infection was established 2 mm proximal to the Test Screw, and a second implant, designated the Infected Screw, was placed. Samples were collected after a further 30 days of infection. (b) Representative photographs taken 30 days after infection induction following 30

days of test implant placement. Scale bar was 2 cm. Yellow circle indicates the Infected Screw, red circle indicates the Test Screw, and yellow arrow indicates the infected area. (c) Bacterial loads on Test Screw and Infected Screw quantified by agar plate assay (n = 6). (d) Representative H&E staining images of decalcified bone sections. Scale bar was 1 mm in the upper panels and 200 μm in the lower panels. (e) Quantification of inflammatory cell area in H&E stained images (n = 3). (f) Representative Trap staining images of decalcified bone section. Scale bar was 1 mm in the upper panels and 200 μm in the lower panels. Yellow arrow indicates the osteoclast active region. (g) Representative Masson staining images of decalcified bone sections. Scale bar was 1 mm in the upper panels and 200 μm in the lower panels. (h) Quantification of collagen deposition in Masson stained images (n = 3). (i) Representative methylene blue-basic magenta staining images of undecalcified bone sections. Scale bar was 1 mm in the upper panels and 200 μm in the lower panels. Yellow arrow indicates the bone erosion phenomenon. (j) Micro-CT 3D reconstructed images of the femur around the Test and Infected Screws. The scale bar was 1 mm. The yellow implant indicated the Infected Screw and the red implant indicated the Test Screw. (k) BV/TV of the Test Screw quantified from Micro-CT three-dimensional reconstructed images (n = 3). (l) BV/TV of the Infected Screw quantified from Micro-CT three-dimensional reconstructed images (n = 3). (m) BMC of the Test Screw quantified from Micro-CT three-dimensional reconstructed images (n = 3). (n) BMC of the Infected Screw quantified from Micro-CT three-dimensional reconstructed images (n = 3).

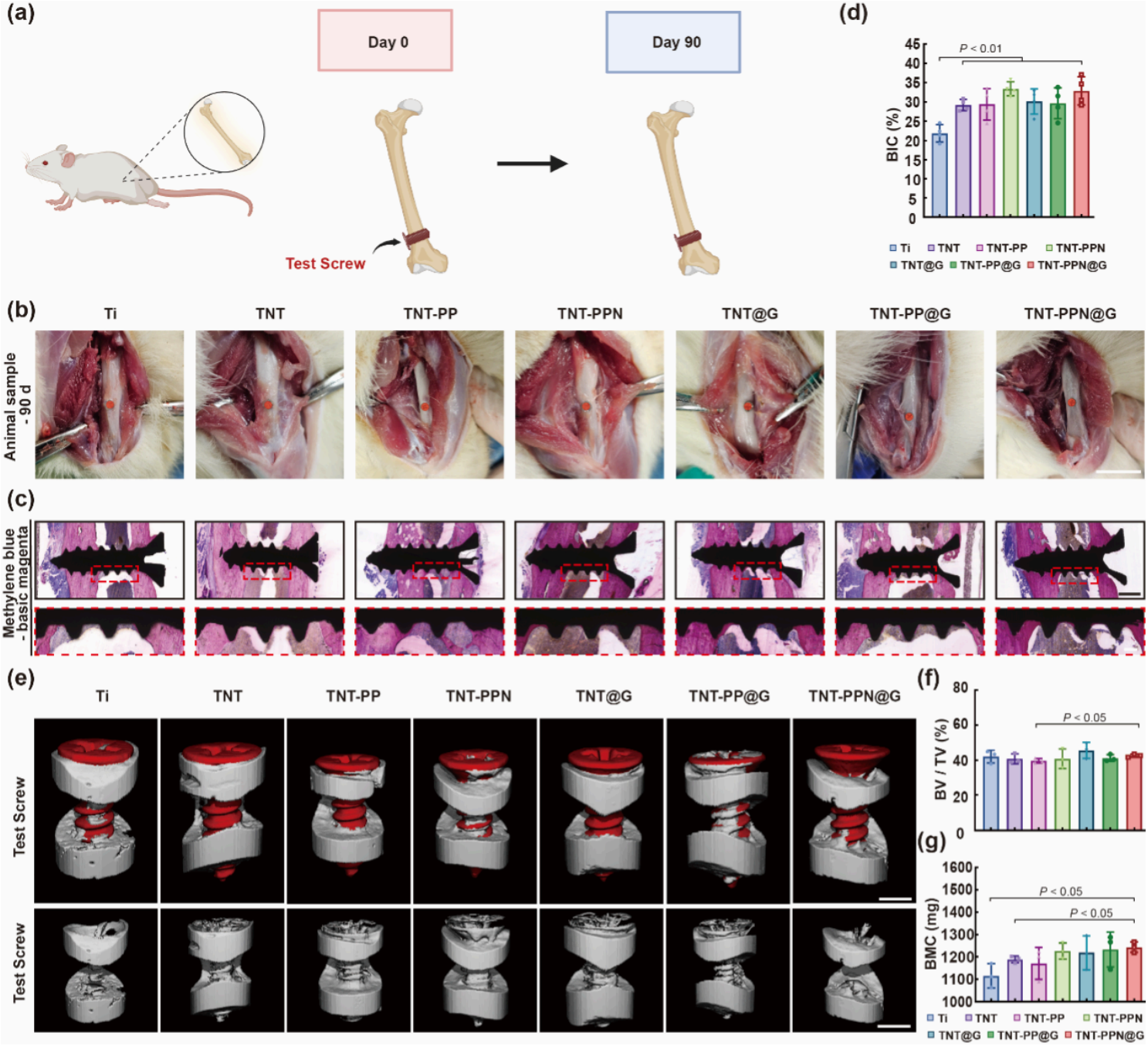

Figure 7

***In vivo* osseointegration in a non-infection SD rat model.** (a) Schematic of the experimental design. 90 days after implantation of the Test Screw into the rat femur, samples were collected. (b) Representative photographs taken after 90 days of test implant placement. Scale bar was 2 cm. Red circle indicates the Test Screw. (c) *In vivo* exploration of biocompatibility after implantation with 90-day Test Screws. Representative methylene blue-basic magenta staining images of undecalcified bone sections. Scale bar was 1 mm in the upper panels and 200 μm in the lower panels. (d) Quantitative analysis of bone-implant contact (BIC) around the Test Screw (n = 4). (e) Micro-CT 3D reconstructed images of the femur around the Test Screw. The scale bar was 1 mm. The red implant indicated the Test Screw. (f) BV/TV of the Test

Screw quantified from Micro-CT three-dimensional reconstructed images (n = 3). (g) BMC of the Test Screw quantified from Micro-CT three-dimensional reconstructed images (n = 3).

Supplementary Files

This is a list of supplementary files associated with this preprint. Click to download.

- SupportingInformation1114.docx
- SupportingInformation1117.docx